SYSTEMS, SCIENCE AND SOFTWARE

SSS-R-77-3349

SEISMIC GROUND MOTION FROM FREE-FIELD AND UNDERBURIED EXPLOSIVE SOURCES

J. T. CHERRY
T. G. BARKER
S. M. DAY
P. L. COLEMAN

FINAL REPORT

SPONSORED BY
ADVANCED RESEARCH PROJECTS AGENCY
ARPA ORDER No. 2551

This research was supported by the Advanced Research Projects Agency of the Department of Defense and was monitored by AFTAC/VSC, Patrick Air Force Base, Florida, 32925, under Contract No. F08606-75-C-0045.

JULY 1977

P. O. BOX 1620, LA JOLLA, CALIFORNIA 92038, TELEPHONE (714) 453-0060

AFTAC Project Authorization No. VELA T/6712/B/ETR

Program Code No. 6F10

Effective Date of Contract: May 1, 1975

Contract No. F08606-75-C-0045

Principal Investigator and Phone No.
Dr. John M. Savino (714) 453-0060, Ext. 453

Project Scientist and Phone No.
Dr. Ralph W. Alewine, III (703) 325-8484

UNCLASSIFIED

SECURITY CLASSIFICATION OF THIS PAGE (When Data Entered)

REPORT DOCUMENTATION PAGE

READ INSTRUCTIONS BEFORE COMPLETING FORM

1. REPORT NUMBER

2. GOVT ACCESSION NO.

3. RECIPIENT'S CATALOG NUMBER

4. TITLE (and Subtitle)

(16) SEISMIC GROUND MOTION FROM FREE-FIELD AND UNDERBURIED EXPLOSIVE SOURCES,

(9) TYPE OF REPORT & PERIOD COVERED

Final Report,

(14) PERFORMING ORG. REPORT NUMBER

SSS-R-77-3349

7. AUTHOR(s)

(10) J. T. Cherry, S. M. Day
T. G. Barker, P. L. Coleman

CONTRACT OR GRANT NUMBER(s)

Contract No.
F08606-75-C-0045

9. PERFORMING ORGANIZATION NAME AND ADDRESS

Systems, Science and Software
P. O. Box 1620
La Jolla, California 92038

10. PROGRAM ELEMENT, PROJECT, TASK AREA & WORK UNIT NUMBERS

Program Code No. 6F10
ARPA Order No. 2551

11. CONTROLLING OFFICE NAME AND ADDRESS

VELA Seismological Center
312 Montgomery Street
Alexandria, Virginia 22314

(11) 12. REPORT DATE

Jul[redacted]77

13. NUMBER OF PAGES

44

(12) 51 p.

14. MONITORING AGENCY NAME & ADDRESS (if different from Controlling Office)

(15) F08606-75-C-0045,
ARPA Order-2551

15. SECURITY CLASS. (of this report)

Unclassified

15a. DECLASSIFICATION/DOWNGRADING SCHEDULE

16. DISTRIBUTION STATEMENT (of this Report)

Approved for Public Release, Distribution Unlimited.

17. DISTRIBUTION STATEMENT (of the abstract entered in Block 20, if different from Report)

18. SUPPLEMENTARY NOTES

ABSTRACT

19. KEY WORDS (Continue on reverse side if necessary and identify by block number)

Seismic waves
Depth of burial
Explosive source
Laboratory explosion experiments

20. ABSTRACT (Continue on reverse side if necessary and identify by block number)

Small-scale laboratory experiments were conducted and analyzed to study the effect of the proximity of the free surface on the seismic ground motions. Two classes of experiments were done. In one the charges were far from the free-surface and the free-field displacement-time histories were measured. In the second class the charges were near the surface and were either fully contained or formed a crater. The charges were

CONT

DD FORM 1 JAN 73 1473 EDITION OF 1 NOV 65 IS OBSOLETE

UNCLASSIFIED

SECURITY CLASSIFICATION OF THIS PAGE (When Data Entered)

388507

CL

20. ABSTRACT (continued)

0.25 g of PETN in concrete cylinders, 120 cm in diameter and 33 to 60 cm thick. In all experiments displacements were measured 30.5 cm directly below the charges. The experiments produced consistent and repeatable data. A striking feature of the ground motions for the near surface experiments is a large long-period negative pulse which is present whether or not cratering occurred.

The results were studied by comparing to numerical simulations of the experiments using a Lagrangian finite difference program and published properties of the concrete and PETN. The calculations are in good agreement with the laboratory data, providing verification of both the constitutive models and the methods.

The large, long-period negative pulse can be explained in the context of linear elasticity. It is due to the near-field interaction of the spherical wave front with the free surface. Therefore, it does not propagate to the far-field and is not important for teleseismic magnitudes.

TABLE OF CONTENTS

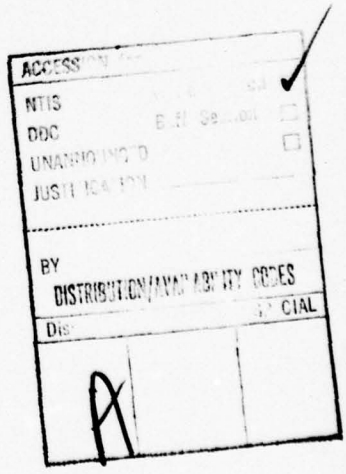

LIST OF ILLUSTRATIONS

LIST OF ILLUSTRATIONS (continued)

I. INTRODUCTION

A critical element in the prediction of teleseismic ground motion from a nuclear explosion is the reflection of the compressional wave from the free surface above the working point. This reflected phase, pP, interferes with the direct wave, P, and significantly affects body wave amplitudes at teleseismic distances.

Most seismological analyses of the pP event assume that the P reflection coefficient is elastic and that the source region is transparent to pP. Recent finite difference simulations of nuclear cratering events by J. Trulio and N. Perl at Applied Theory, Incorporated, have produced a large, low frequency, negative pulse following the direct P wave at emergent angles appropriate for teleseismic P waves. They attribute this pulse to the preferential expansion of the source region toward the free surface and the subsequent closure of cracks above the source.

Unfortunately there are few, if any, near source ground motion records which can be used to verify these assumptions. Both cost and containment limitations prohibit obtaining adequate near source ground motion data from nuclear explosions relevant to the pP issue. Moreover, even if these limitations could be removed, the variation of in situ rock material properties could alter ground motion as much as variations in pP when depth of burial is changed.

In view of the above limitations we have turned to laboratory modeling in order to obtain ground motion data as a function of depth of burial under well controlled conditions. Numerical and analytic models were then used to explain the data.

Two types of experiments were carried out. First we overburied the charge in order to measure the direct (free-field) P wave radiated by the explosion. We will call this class of experiments free-field since the seismic radiation is uncontaminated by the pP event. In the second type of experiment the charge was detonated near a free surface and the direct P wave is contaminated by pP. We will call this class of experiments underburied. It includes as a subset depths of burial which produce craters at the free surface.

One of our objectives was to determine the effect of depth of burial on both body wave and surface wave magnitudes. This requires the capability to analytically continue the results of a close-in numerical simulation to far-field distances.

Rigorous analytic continuation procedures for an explosive source detonated in a halfspace are currently being developed at Systems, Science and Software (S^3) and were not available for this research project. Quantitative estimates of the far-field seismic radiation from our simulations must await the development of this continuation procedure.

In spite of this, the project has contributed greatly to our understanding of the seismic wave field radiated by an explosion in a halfspace. In particular, during the course of this work, we have:

1. developed and demonstrated the capability to design and instrument small scale laboratory model experiments and obtain repeatable displacement time history data from free-field and underburied explosive sources,

2. shown that our numerical models generate displacement time histories which agree with the data obtained from the laboratory model,

3. experimentally determined the difference in displacement time history between free-field and underburied sources at emergent angles from the source which are particularly relevant to body wave magnitude,

4. used numerical and analytic models to determine the physical mechanism behind the generation of the broad negative phase which follows the direct P arrival.

In Section II we present a description of the laboratory model and the results obtained. Section III compares the results of the numerical model with the laboratory data. Section IV provides the analysis of the negative pulse. Section V gives the conclusions and recommendations.

II. THE LABORATORY MODEL

2.1 INTRODUCTION

Free-field and underburied cratering explosions were modeled in the laboratory on a small scale by embedding one-fourth gram spheres of the high explosive, PETN, in concrete cylinders of 120 cm diameter. The bottom end of the cylinders represented the ground surface and the seismic coupling of the charge was determined by measuring the displacement of a point on the top surface directly above the charge. The thickness of the cylinders varied between 33 and 60 cm. The vertical distance between charges and sensors was constant (30.5 cm) for all the experiments. The distance between the charges and the bottom free surface was varied to simulate different depths of burial. The dimensions of the cylinder were selected such that all surfaces except the bottom surface were well beyond the inelastic region surrounding the charge. The top surface, where sensors were located, was always outside the inelastic region surrounding the explosive.

2.2 EXPERIMENTAL DESIGN

The actual configuration is shown in Figure 2.1 and the summary of tests is given in Table 2.1. Each cylinder was used for three shots fired separately with charges spaced in a triangular array. The vertices were at wide enough separation to assure that the inelastic regions for separate shots did not overlap. The gauges were also located at the vertices of a triangle with each gauge directly above a charge. At Vertex 1 horizontal and vertical displacements were measured. Vertical displacement and acceleration were measured at Vertex 2 and only vertical acceleration was measured at Vertex 3. (Only Test 0 deviated from this configuration in that two displacement gauges and an accelerometer were fixed above one charge. This test was a check of the instrumentation.)

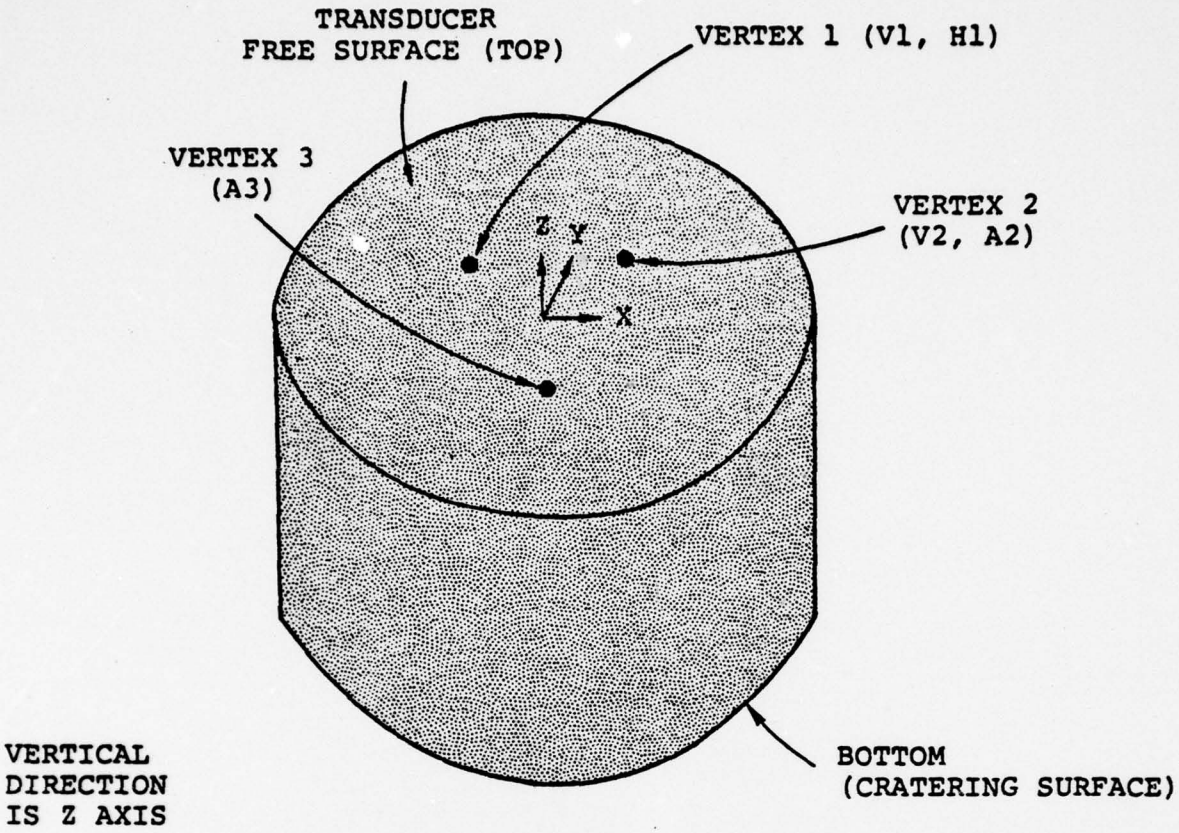

POINT	COORDINATES (X,Y,Z) cm
Vertex 1	(-15.2, 8.7, 0)
Vertex 2	(15.2, 8.7, 0)
Vertex 3	(0, -17.6, 0)
V1, Vertical Displacement Gauge	(-14.0, 8.7, 0)
H1, Horizontal Displacement Gauge	(-16.5, 8.7, -0.5) Sensitive axis || x
V2, Vertical Displacement Gauge	(14.0, 8.7, 0)
A2, Vertical Accelerometer	(16.5, 8.7, 0)
A3, Vertical Accelerometer	(0, -17.6, 0)
Charge 1	(-15.2, 8.7, -31)
Charge 2	(15.2, 8.7, -31)
Charge 3	(0, -17.6, -31)
Cylinder Bottom	(X, Y, -33 or -37 or -60 [Table I])

Figure 2.1. Schematic of the laboratory model. The diameter of the cylinder was 122 cm.

TABLE 2.1

SUMMARY OF DETAILS FOR SEISMIC MODELING EXPERIMENTS

Test No.	Cylinder Thickness (cm)	Distance to Nearest Free Surface (cm)	Distance of Charge Below Gauge (cm)	Crater Surface Dimensions (cm x cm)	Peak Displacement (μm)
0*	60	29.5 (Free-field)	30.5	-	4.5, 5.0, 6.7
1	37	6.5 (Underburied)	30.5 Vertex 1	-	5.3
2	37	6.5 (Underburied)	30.5 Vertex 2	-	3.5
3	37	6.5 (Underburied)	30.5 Vertex 3	-	5.5
4	60	29.5 (Free-field)	30.5 Vertex 1	-	4.9
5	60	29.5 (Free-field)	30.5 Vertex 2	-	3.3
6	60	29.5 (Free-field)	30.5 Vertex 3	-	3.1
7	33	1.75 $\pm$ 0.08 (Underburied, Crater)	31.3 Vertex 1	7 x 10	7.0
8	33	1.43 (Underburied, Crater)	31.6 Vertex 2	6 x 7	4.9
9	33	1.91 (Underburied, Crater)	31.1 Vertex 3	9 x 11	8.5

*Instrument Check

The concrete cylinder was made of a material called "high-early" concrete. This designation refers to the fact that it attains a high strength soon after setting. It has a density of 2.52 gm/cm^3 and unconfined compressive strength of 345 x 10^6 dynes/cm^2 (345 bars) with low porosity and high water saturation.

The design of the explosive charge, and in fact the scale of the entire experiment, was fixed by the need to use a source that was very nearly spherically symmetric. Such a source was available from Stanford Research Institute (SRI) in the configuration shown in Figure 2.2. Tests at SRI have shown that these charges yield a shock wave which is spherically symmetric to within two percent [Erlich, 1975]. Each charge is a one-fourth gram of PETN powder packed to a density of 1 gm/cm^3. The explosive is encapsulated in a lucite shell and can be detonated by an explosive bridge wire at the center.

The principal sensors were eddy-current displacement gauges supplied by Kaman Sciences, Colorado Springs, Colorado. Each unit's output varies linearly with distance between the probe's tip and a small piece of aluminum foil fixed with epoxy to the concrete surface. These transducers have rather low output levels, 2 mV/μm, but they have the advantages that they do not touch the concrete and their response extends to 50 kHz (3 db). To supplement the displacement gauges, two accelerometers supplied by Endevco (San Juan Capistrano, California) were used also. The accelerometers had a range of $\pm$ 50,000 g's (5 x 10^5 m/sec^2), a sensitivity of 10 μV/g and resonant frequencies above 150 kHz. For these experiments the acceleration risetimes are roughly 4 μs which corresponds to 80 kHz. Therefore, the resonance may be partially excited and the acceleration signals should be treated as upper limits for actual motion of the surface.

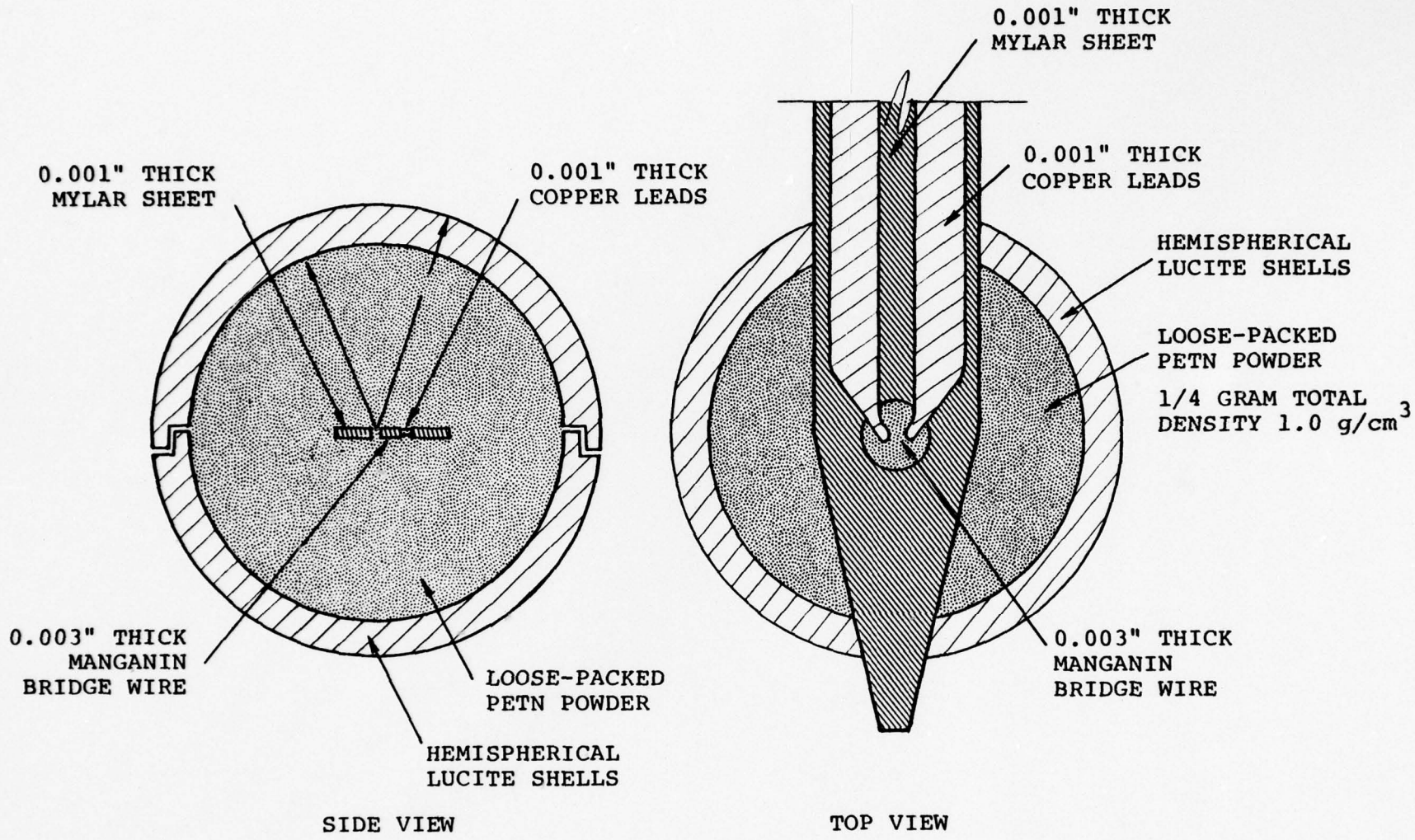

Figure 2.2. Cross-sectional diagrams of spherical explosive source.

2.3 FREE-FIELD EXPERIMENTS

In order to gain confidence in the experimental technique, the first experiment (Test 0) was designed to demonstrate repeatability of the measurements. Two displacement gauges and an accelerometer were in close proximity directly above one charge in order to see if the three independent transducers would give similar responses to the same seismic motion. The resulting measurements are shown in Figure 2.3. The data from the accelerometer is integrated twice to give displacement. The direct displacement responses were in fact quite similar, showing an arrival time of 92 μs, risetime of 15 μs, peak motion of 5 μm and full width at half maximum of about 20 μs. The double integration of acceleration data results in a slightly higher displacement, which is expected because of the partial excitation of resonance of the acceleration gauges which was discussed in the preceding section. Also, the double integration of the acceleration signal is subject to a gradually increasing displacement at late time.

The results of free-field Tests 4 and 5 (Table 2.1) are shown in Figures 2.4 and 2.5. For these tests, displacement gauges were located directly above each charge. In addition to the primary vertical displacement pulse, which arrives at about 95 μs, the records also show the arrival of a more slowly traveling wave at approximately 160 μs and reflection from the bottom and sides of the cylinder at 270 μs. The wave arriving at 160 μs, shown on H1 in Figure 2.4, may be a shear wave generated by the explosive. If this is the case, then the source for Test 4 may not be as pure a center of dilatation as SRI reported. However, a more likely explanation is that the S waves are generated by asymmetries in the emplacement cavity (the charges were placed in drill holes which were then stemmed with grout).

In order to obtain the best measure of free surface displacement for these tests and to determine the experimental variability, all direct measures of free surface displacement

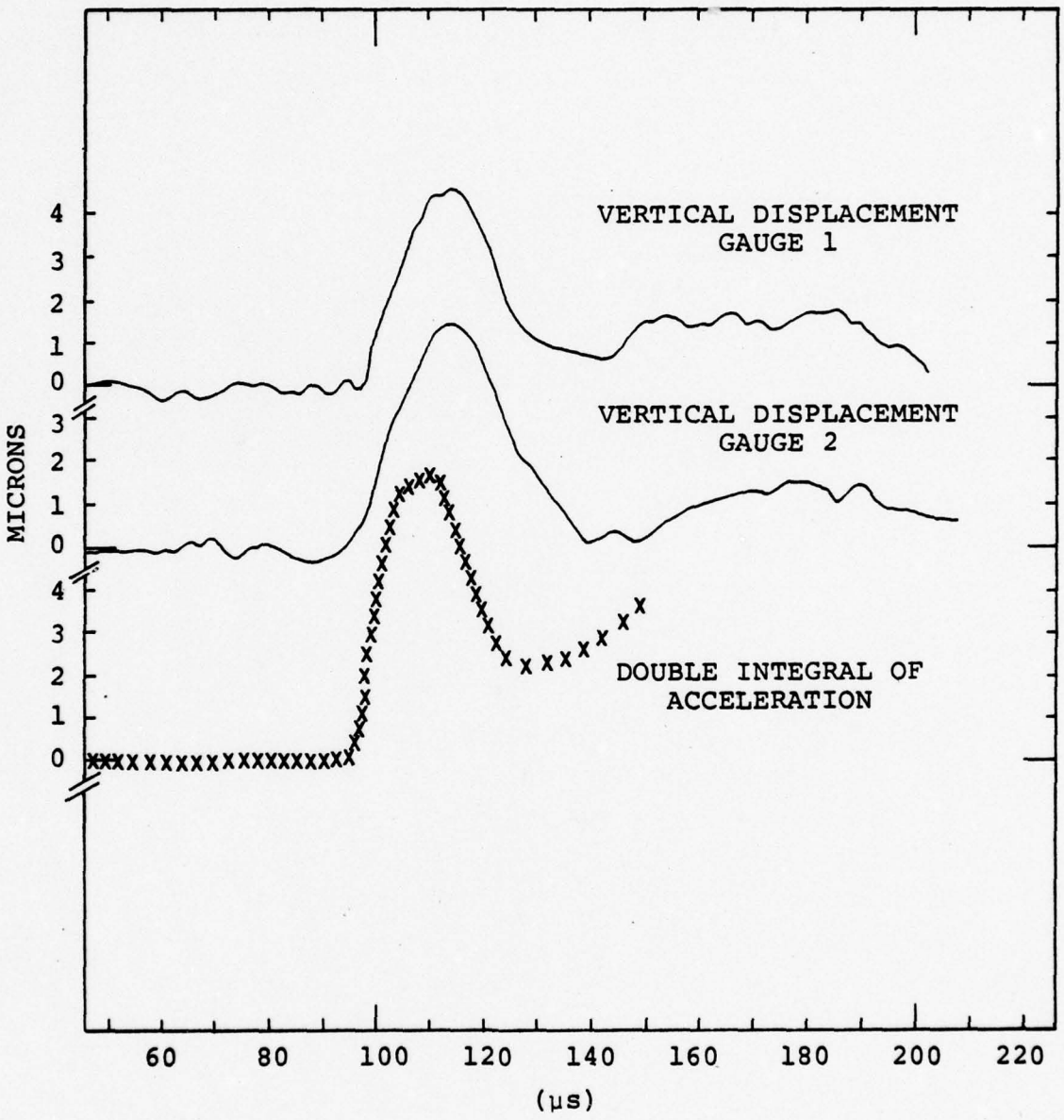

Figure 2.3. Free surface displacements for instrument checkout (Test 0).

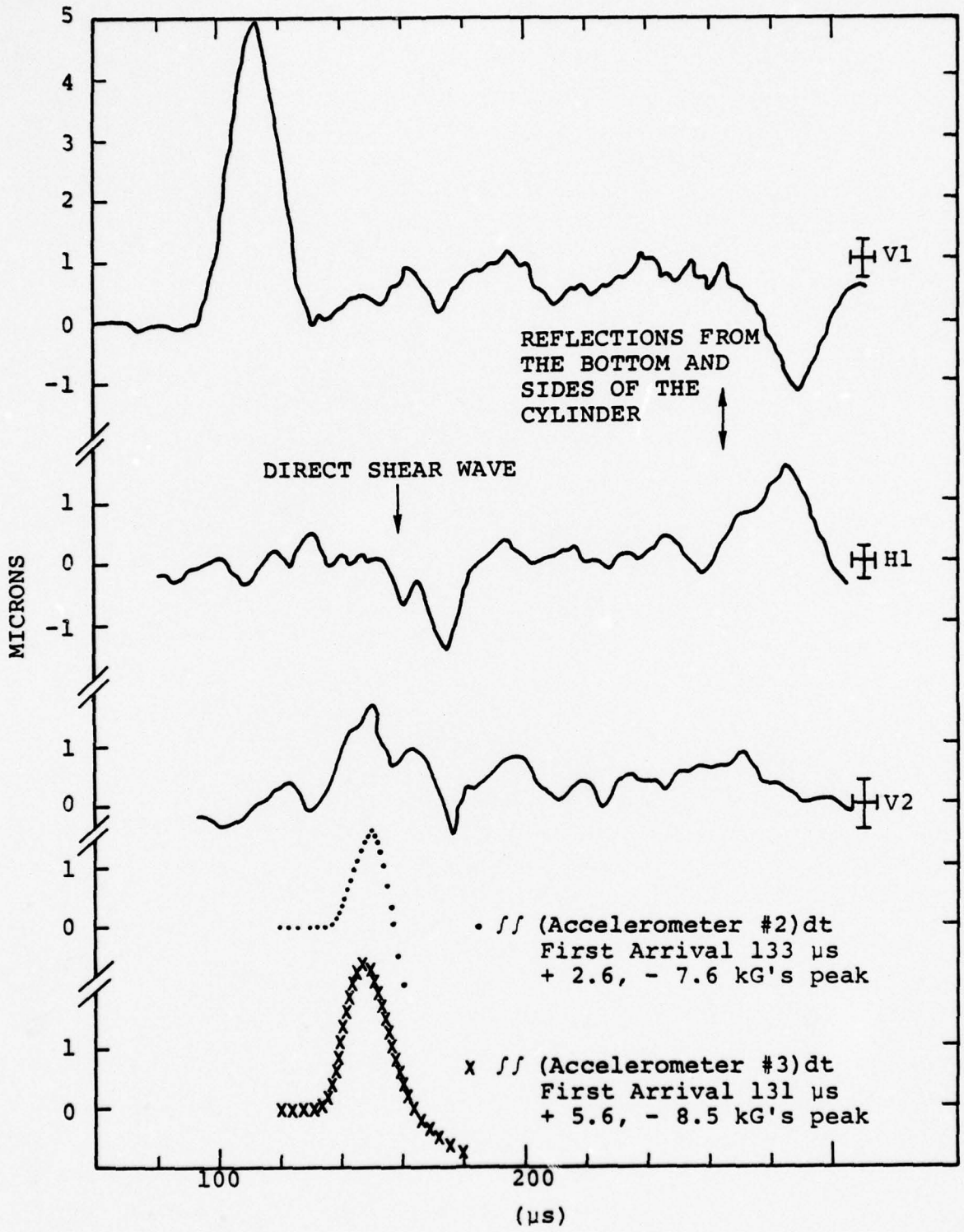

Figure 2.4. Displacement data for Test 4 where the charge was emplaced under Vertex 1. The vertical and horizontal displacement records at Vertex 1 and the vertical displacement record at Vertex 2 are shown. Also plotted are the doubly integrated accelerometer records from Vertices 2 and 3. For the accelerometer records the time of first arrival and first peak and trough accelerations are indicated.

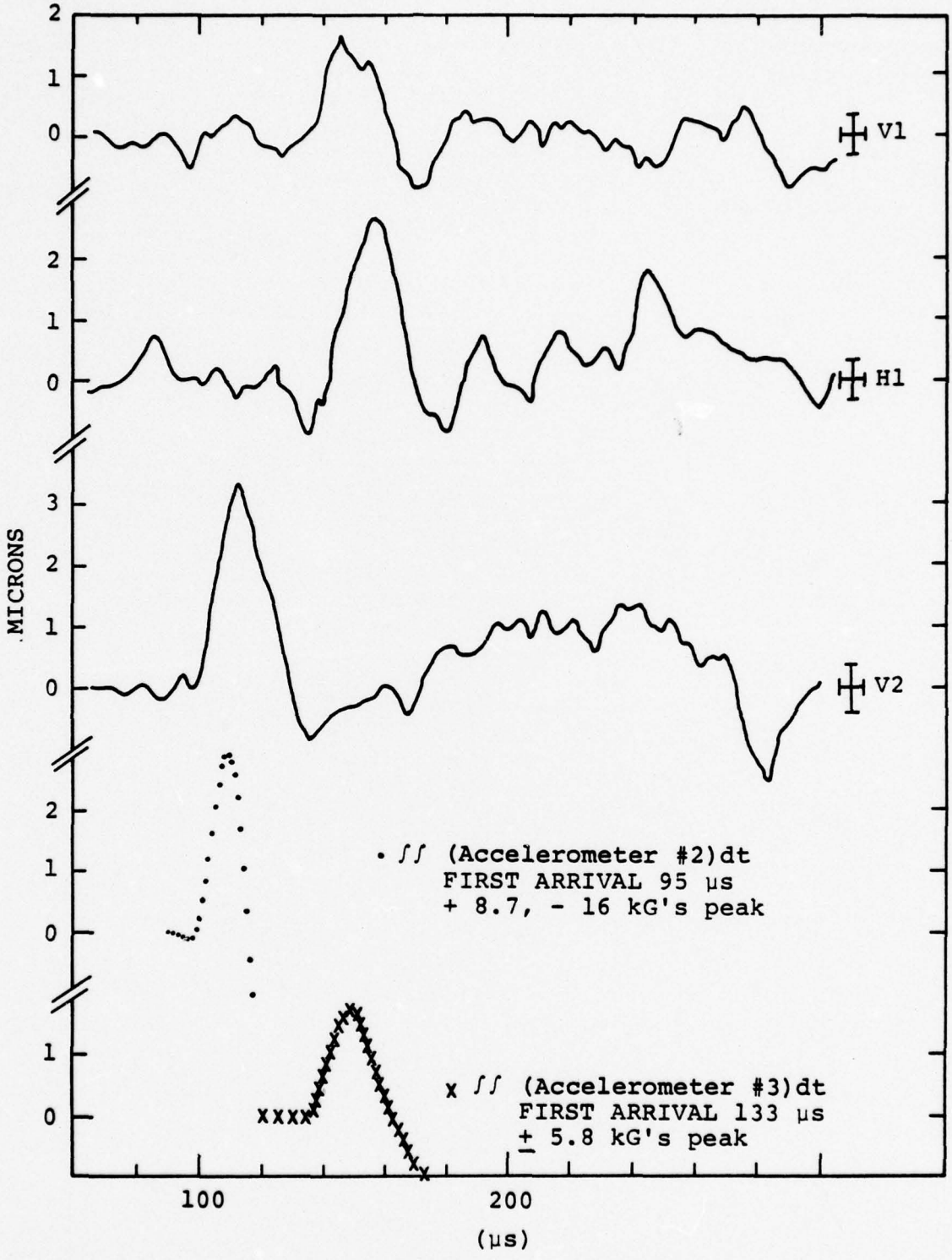

Figure 2.5. Displacement data for Test 5. Similar to Figure 2.4 except that now the charge is located under Vertex 2.

from contained shots were superimposed and are shown in Figure 2.6. The repeatability in the shape and magnitude is very good for these four records, two of which were measured from the same test with different gauges (Test 0) and two of which were measured from Tests 4 and 5. Our estimate of the total amplitude error due to the data collection process was $\pm$ 0.3 μm. The fact that some amplitude variations in Figure 2.6 are larger than that is probably due to slight variations in the coupling between the concrete and charge surfaces. The results from Test 5 appear anomalous in terms of both the maximum and minimum amplitudes of the displacement pulse. If we ignore the results from this test, then we obtain average estimates for the peak, minimum and static displacements of 4.8 μm, 0.5 μm and 1.0 μm for free-field source.

2.4 UNDERBURIED SOURCES

The results shown in Figure 2.6 give displacement records for the free-field shots, i.e., the displacement reaches a static value before the arrival of a free surface reflection. We now present results for the underburied sources where the reflections from the bottom free surface contaminates the direct wave from the source.

Figures 2.7 and 2.8 show displacement records from Tests 1 and 2 (Table 2.1). In these tests the bottom free surface was 6.5 cm below the charge. The reflection from this surface arrives at 135 μm and is clearly evident on record V1 in Figure 2.7 and record V2 in Figure 2.8. Following the reflected wave, which appears to be an inverted replica of the direct wave, there is a broad negative pulse. This negative pulse attains its minimum value at 210 μs for both tests.

Figures 2.9 and 2.10 show displacement records from Tests 7 and 8 (Table 2.1). For these tests the bottom free surface was 1.75 cm and 1.43 cm below the charge. Craters

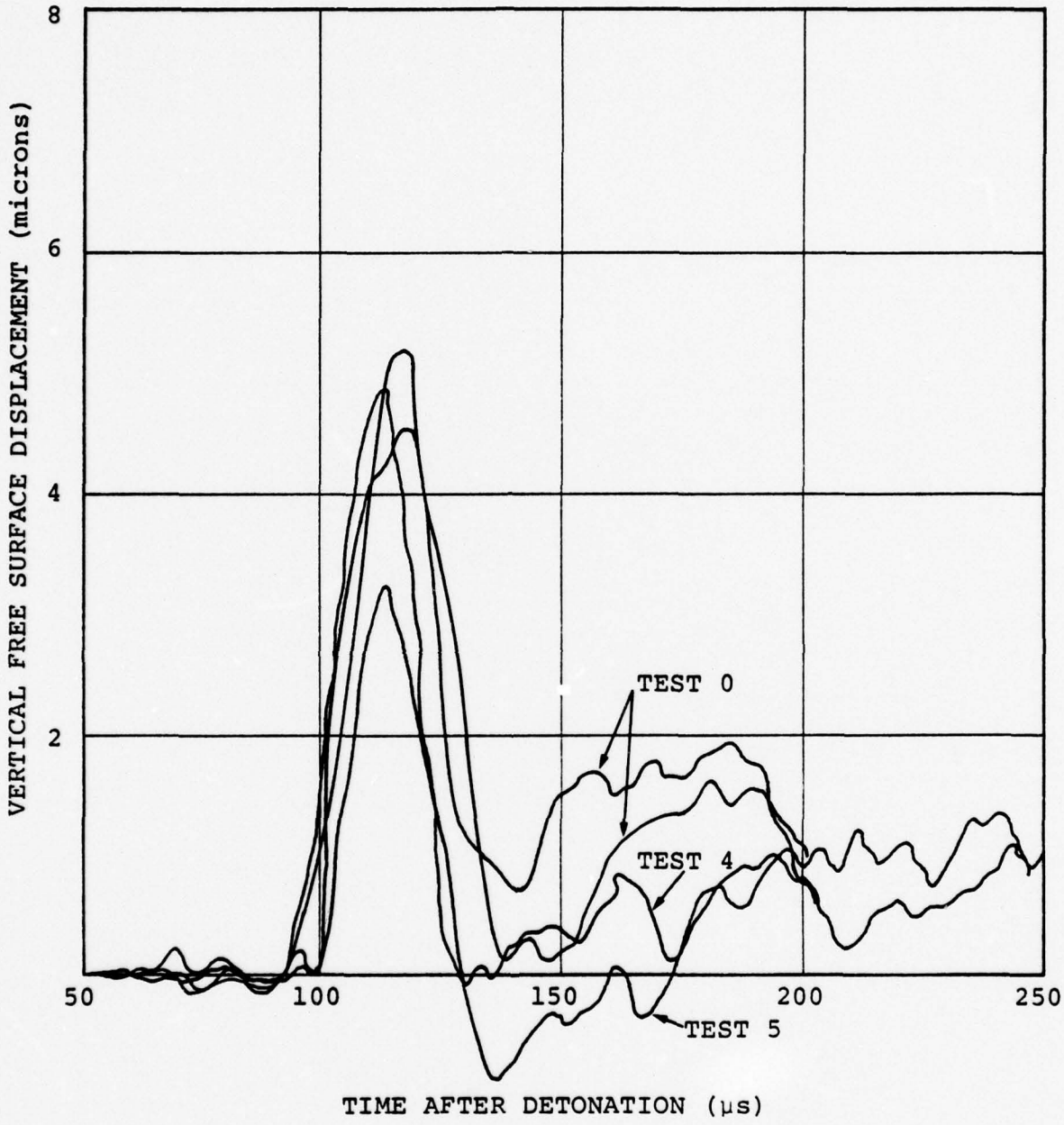

Figure 2.6. Superposition of direct displacement measurements for the free-field tests.

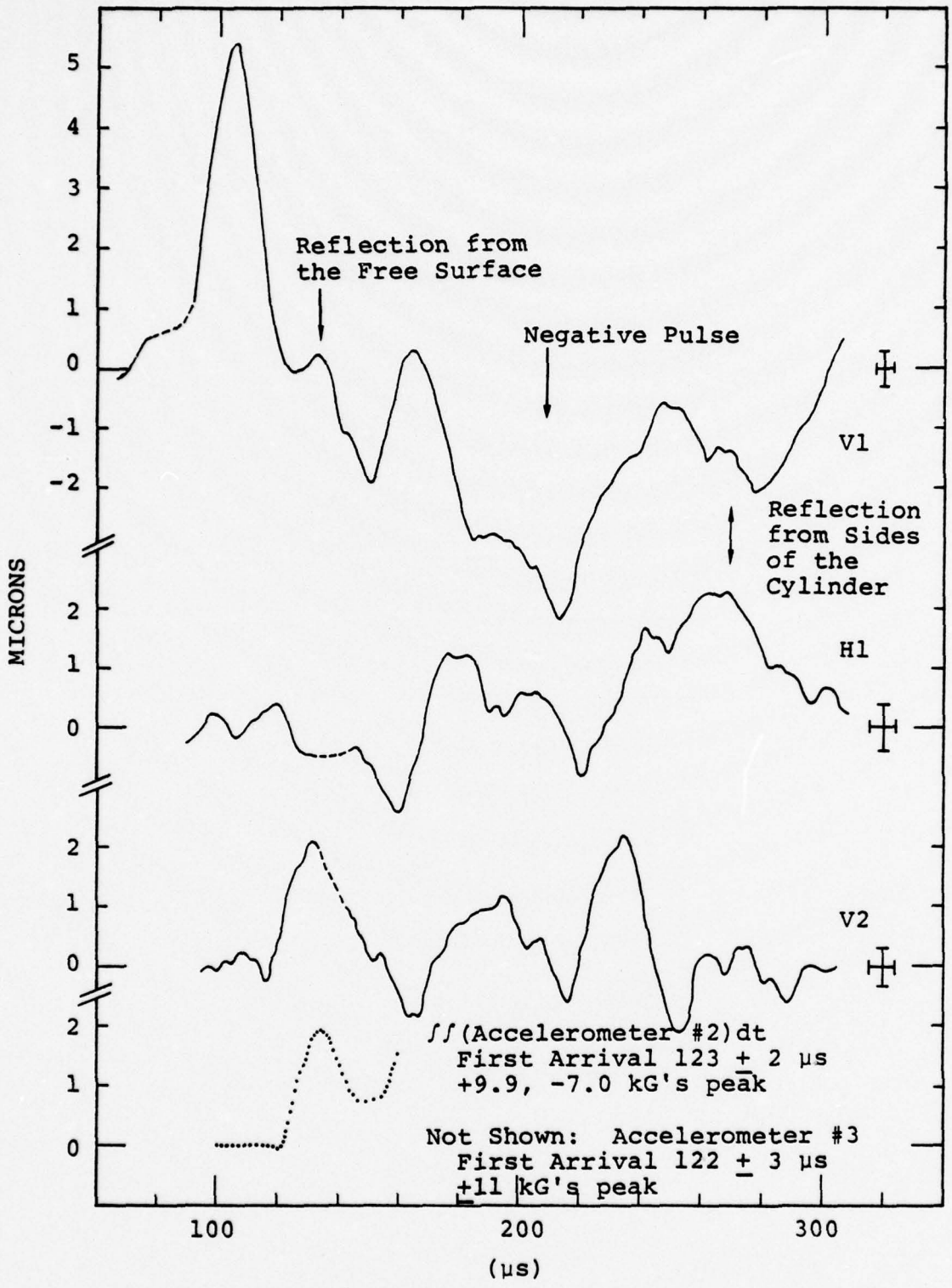

Figure 2.7. Displacement data for Test 1. Vertex 1 is directly above the shot. The vertical and horizontal displacement records at Vertex 1 and vertical displacement record at Vertex 2 are shown. Also plotted is the doubly integrated accelerometer record from Vertex 2. For the accelerometer records at Vertices 2 and 3 the first arrival and first peak and trough accelerations are indicated.

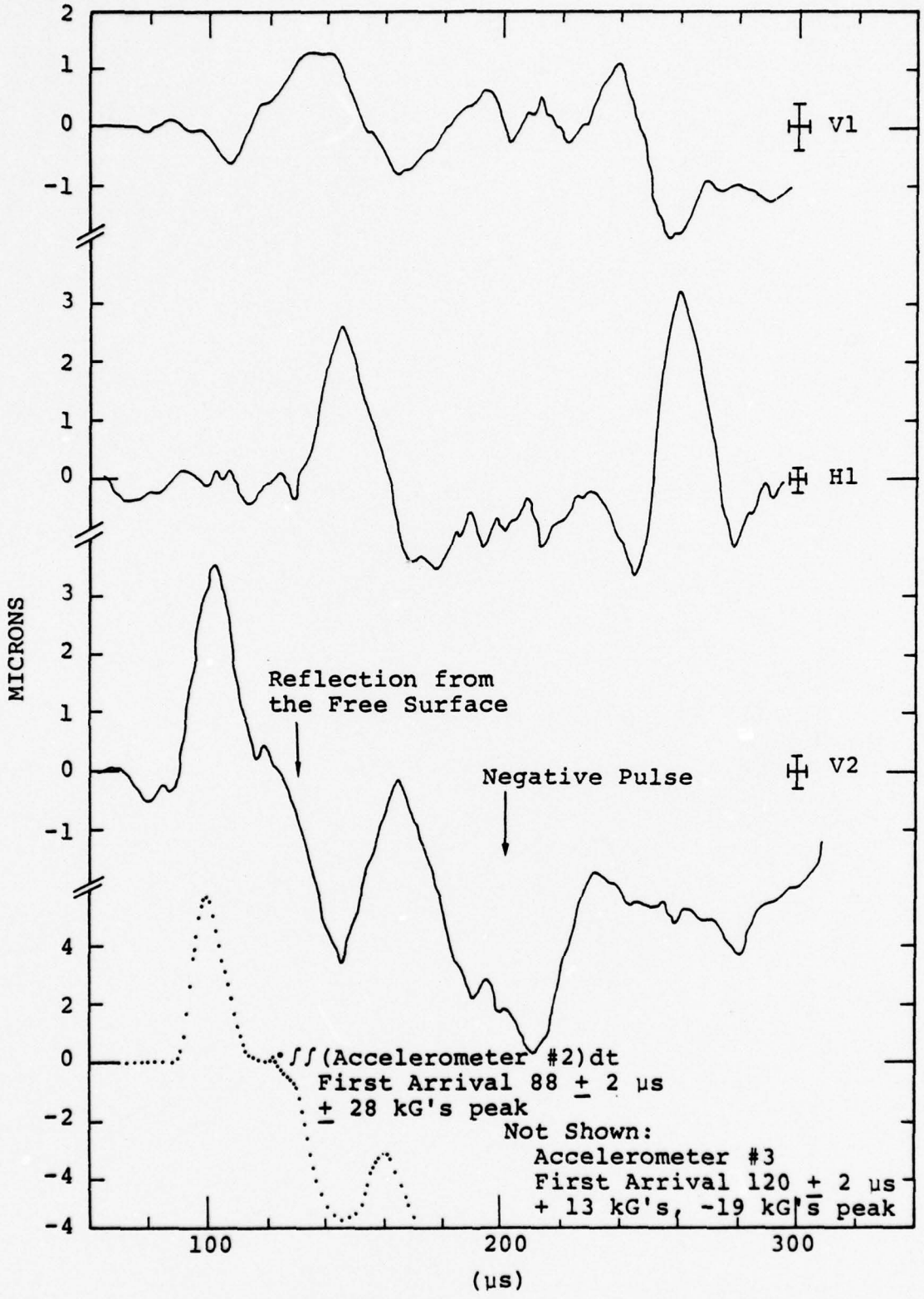

Figure 2.8. Displacement data for Test 2. Similar to Figure 2.7 except here the charge was located under Vertex 2.

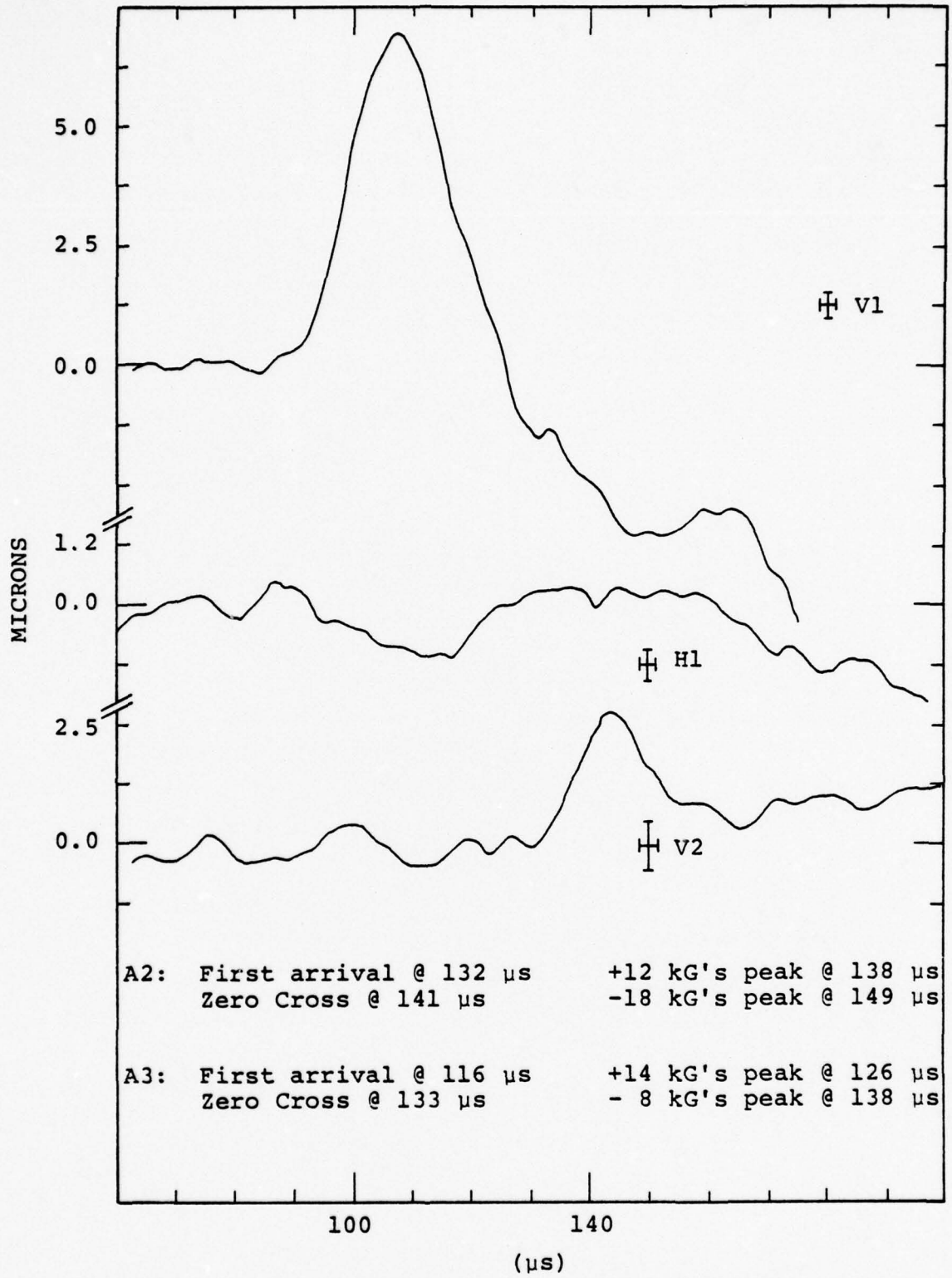

Figure 2.9. Displacement data for Test 7 with charge located under Vertex 1. The vertical and horizontal displacement records at Vertex 1 and the vertical displacement record at Vertex 2 are shown. Instead of complete accelerometer records from Vertices 2 and 3, times are given for the first arrival and the zero crossing. Also indicated are the magnitudes and times of the first peak and trough.

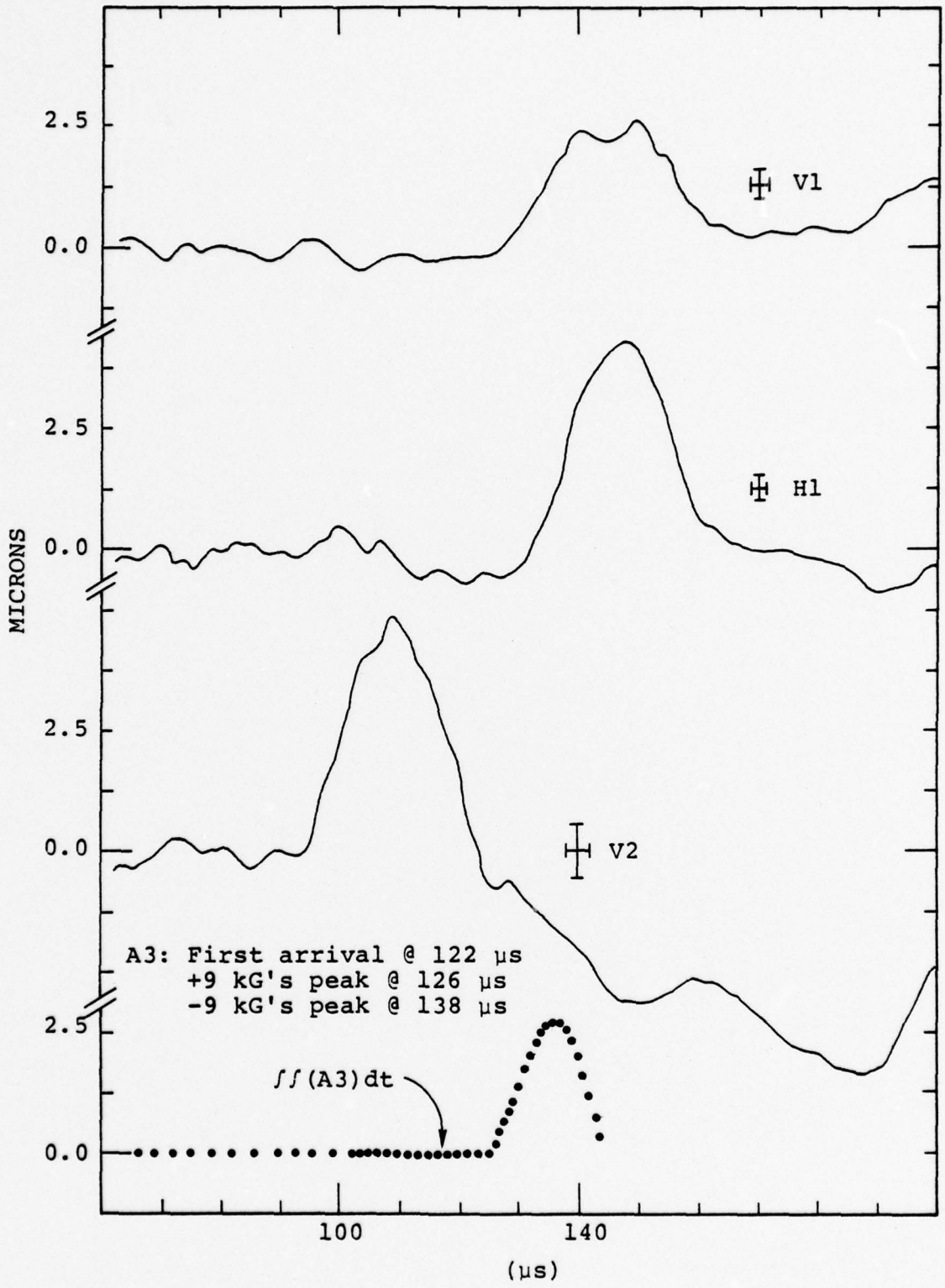

Figure 2.10. Displacement data for Test 8. Similar to Figure 2.9 except here the charge was under Vertex 2.

were produced at this surface for both tests. The crater dimensions are given in Table 2.1.

At these shallow depths of burial, the broad negative pulse dominates the late time portion of the seismogram. This is illustrated further in Figure 2.11, which compares displacement records at stations directly above the charge for Tests 4 and 8.

2.5 SUMMARY

1. We have demonstrated that laboratory model experiments can produce extremely useful and repeatable displacement time histories that are relevant to teleseismic coupling.

2. We have shown that the broad negative pulse, which follows the P arrival for the underburied shots, is not peculiar to the cratering mode. This event occurred for all underburied shots including those that did not spall at the free surface and/or crater.

3. Our experimental results indicate that a necessary condition for the occurrence of the negative phase is that the shot be detonated near the surface in a halfspace. Nonlinear material behavior at the free surface is not required.

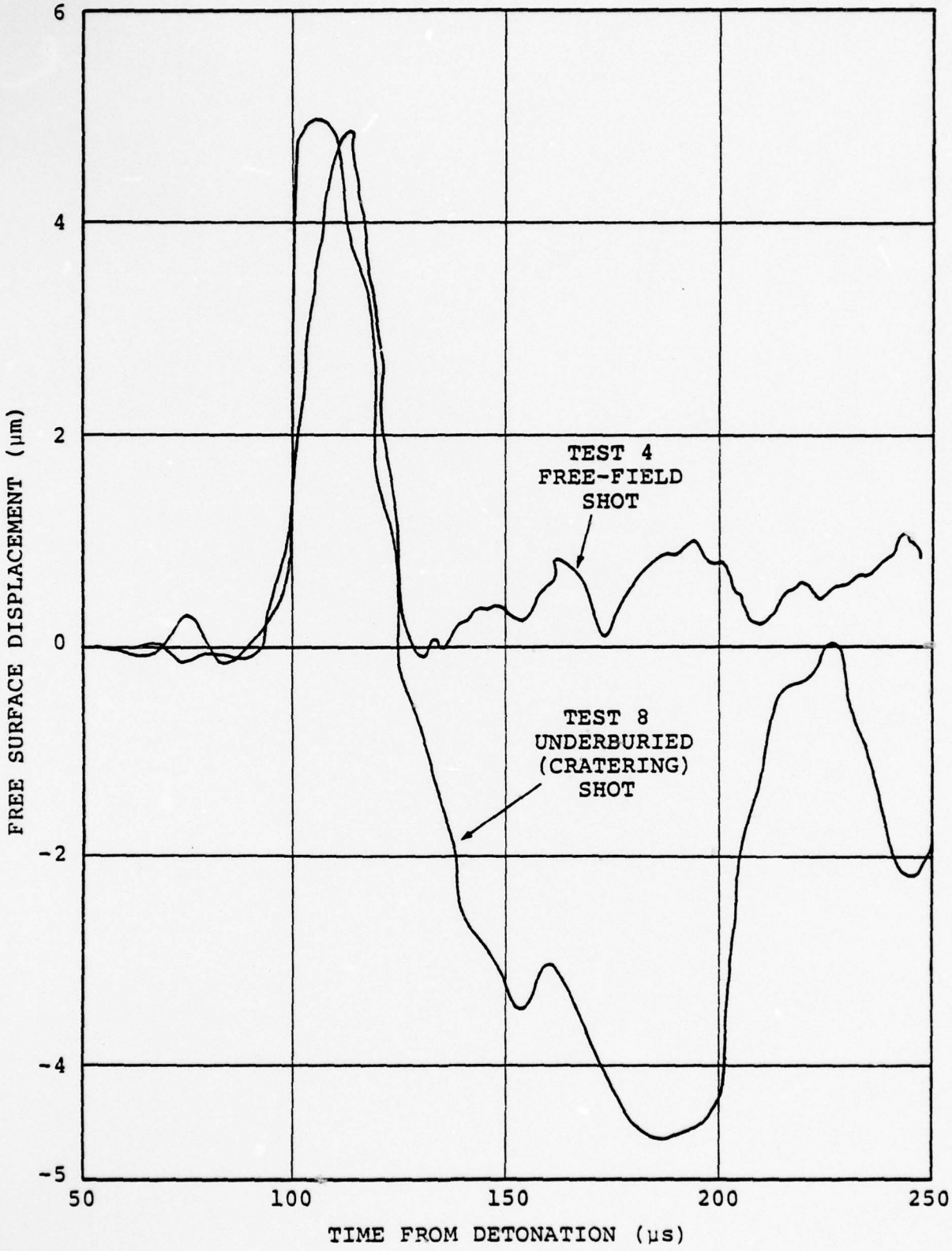

Figure 2.11. Comparison of typical records for displacement from free-field and underburied (cratering) shots.

III. THE NUMERICAL MODEL

3.1 INTRODUCTION

Numerical simulations of the free field and underburied shots were performed with Lagrangian finite difference codes using constitutive models for shear and tension failure reported by Cherry, et al., (1975). However, in order to permit pP to arrive as a distinct phase a modification to the tension failure portion of the model was required. Therefore we will present those features of the model required to understand the modification.

A fundamental material property in the model is the fracture locus

$$Y = Y(\bar{P}) = Y_o + \frac{Y_m}{\bar{P}_m} \bar{P} \left(2 - \frac{\bar{P}}{\bar{P}_m}\right) \quad ,$$

where

$$Y = (3 J_2')^{1/2} \quad ,$$

$$\bar{P} = P - \frac{1}{2}\left(\frac{J_3'}{2}\right)^{1/3} \quad .$$

J_2' and J_3' are the second and third deviatoric invariants and P is the hydrodynamic component of the stress tensor.

Cherry, et al., (1975) assumed that at any stress state, $\bar{P}$, tension failure would occur if the following conditions were simultaneously satisfied.

1. The fracture locus was exceeded by the unadjusted stress deviators.
2. Any principal stress was tensile.

This model produced an extraordinary match to the free-field data. However pP was unable to propagate through the region around the cavity containing open tension fractures. This was not consistent with the experimental data e.q., the result shown in Figure 2.7. Therefore we added a third condition which required that $\bar{P}$ should be tensile, i.e.,

$$\bar{P} = \leq 0 \tag{3.1}$$

where $\bar{P}$ is negative in tension.

With this third condition the match to the free-field data deteriorated somewhat. However the overall agreement with both the free-field and underburied shots was more than satisfactory.

3.2 SIMULATION OF THE EXPERIMENTS

The calculated ground motion 30.5 cm from the free-field source is shown in Figure 3.1 along with all the free-field experimental data. Two free-field calculations are presented in the figure, one in which tension failure was permitted only if $\bar{P}$ was tensile and one in which tension failure could occur for any value of $\bar{P}$; i.e., with and without Equation (3.1) included in the tension failure model. The reduced velocity potential (RVP) transforms for the two calculations are shown in Figure 3.2 and compared to the RVP from Test 4.

We see from these two figures that agreement between simulation and data is excellent when Equation (3.1) is not included in the tension failure model. We then used this model to simulate Test No. 1, with the charge buried 6.5 cm below the free surface. The result is shown in Figure 3.3 which gives the calculated displacement history 30.5 cm below the charge. Comparing this calculation with the data shown

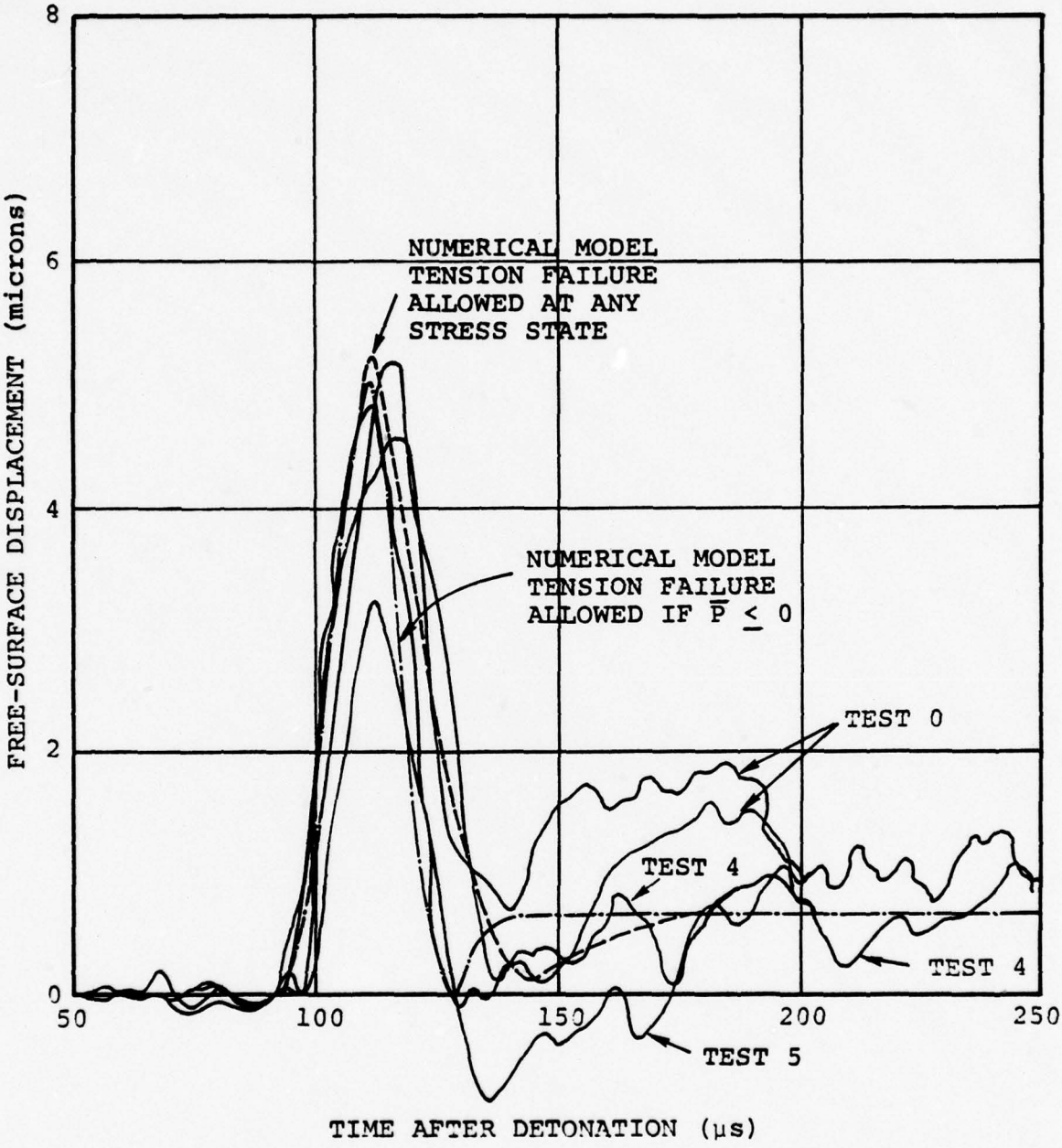

Figure 3.1. Comparison of measured and numerically simulated displacements.

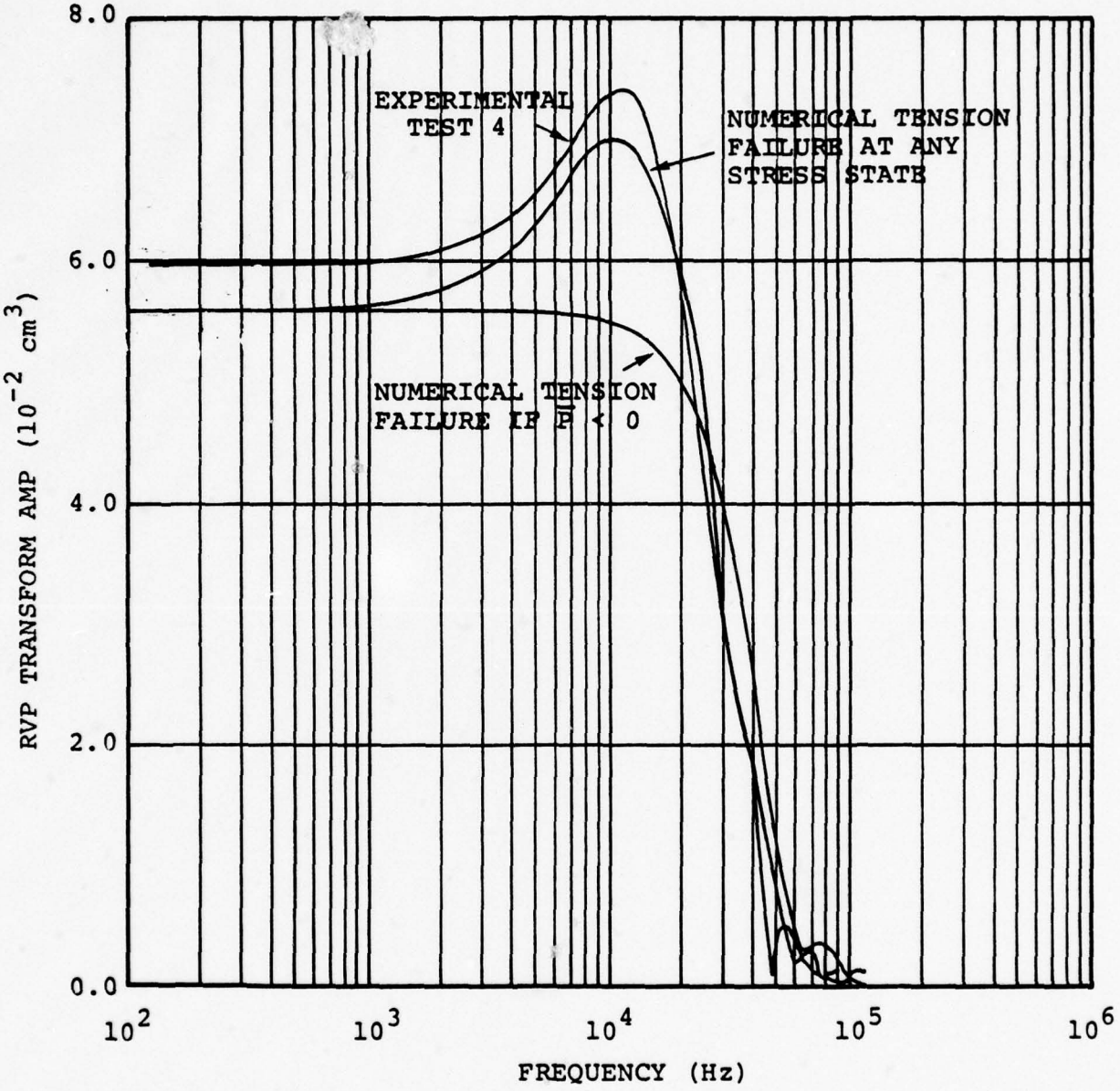

Figure 3.2. Comparison of experimental and numerically simulated source functions expressed as RVP transforms.

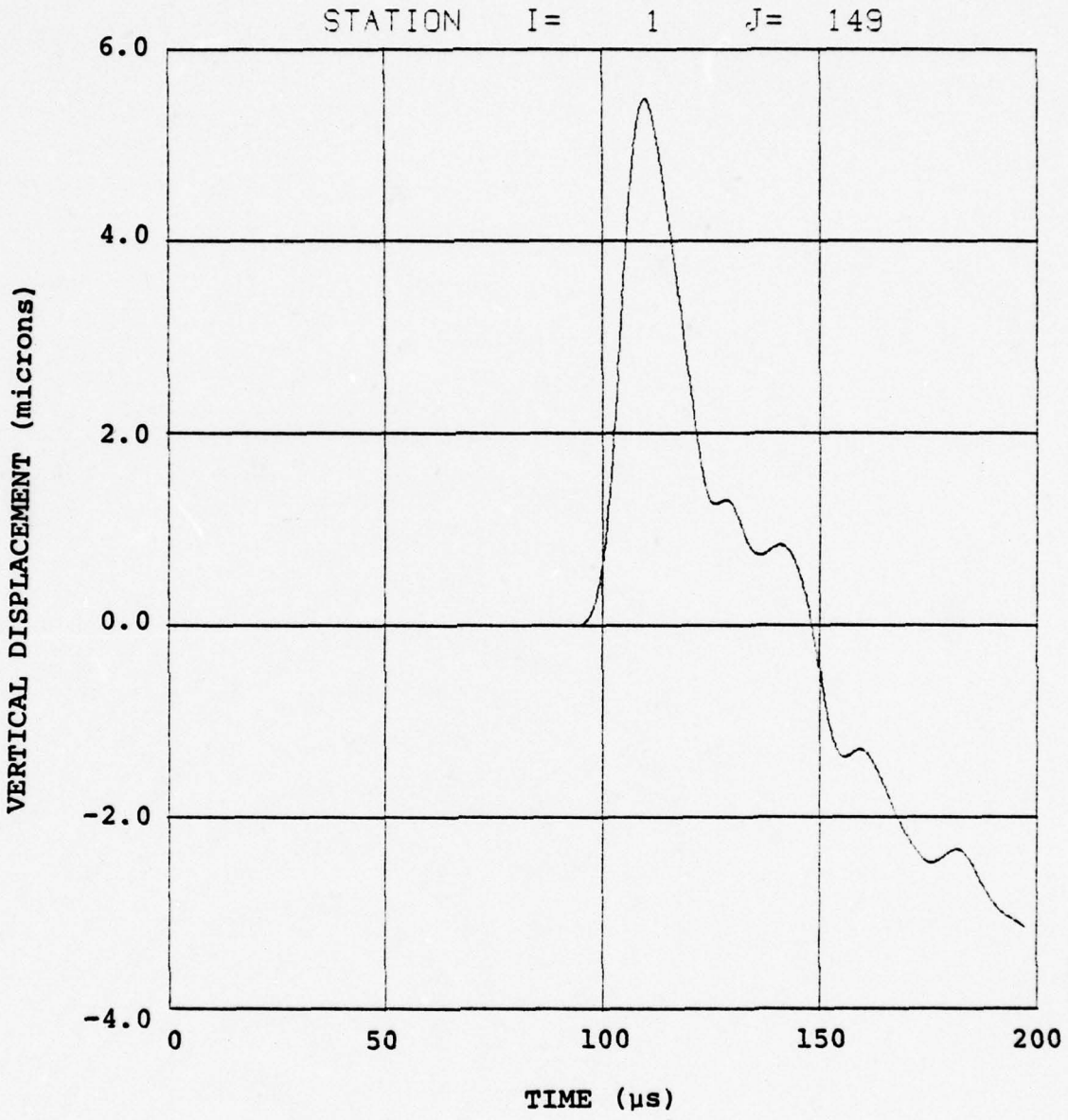

Figure 3.3. Simulation of Test 1 where the displacement is calculated 30.5 cm directly below the shot. Note the absence of pP which arrives in the experimental data (Figure 2.7) at 150 μs. The source region is opaque to this event because of open tension fractures.

in Figure 2.7, we note the absence of the pP arrival at 150 μs in the calculation. The negative phase is present but not pP.

The absence of pP in the calculation is due to tension fractures which surround the cavity and which remain open at late time. The late time crack porosity distribution is shown in Figure 3.4. This region is opaque to pP and will remain opaque as long as the fractures remain open.

Figures 3.5 and 3.6 compare simulations and data for Test 1 and Test 8 respectively with Equation (3.1) included in the tension fracture model. The pP event is now a distinct arrival in Test 1 and the overall agreement between the simulation results and the data is quite acceptable.

3.3 MATERIAL PROPERTIES

The pressure component of the stress tensor for the concrete was calculated using

$$P = A\mu + B\mu^2$$

where $\mu = \frac{\rho}{\rho_o} - 1$. No ambient air-filled porosity was assumed to exist in the concrete.

The parameters defining the material properties for the concrete are listed in Table 3.1. These parameters were derived from measurements of P-wave velocity, V_p, density, ρ, and the unconfined compressive strength, Y_u. The values for shear modulus, G, and bulk modulus, A, were determined from V_p and ρ by assuming a Poisson's ratio of 0.1. Additional characteristics were obtained from data available for DF-5a grout (Cherry and Petersen, 1970).

The results of Finger, et al., [1976], provide the values for the constants in the JWL equation of state for the products of detonation of PETN and for their isentropic expansion. These equations are

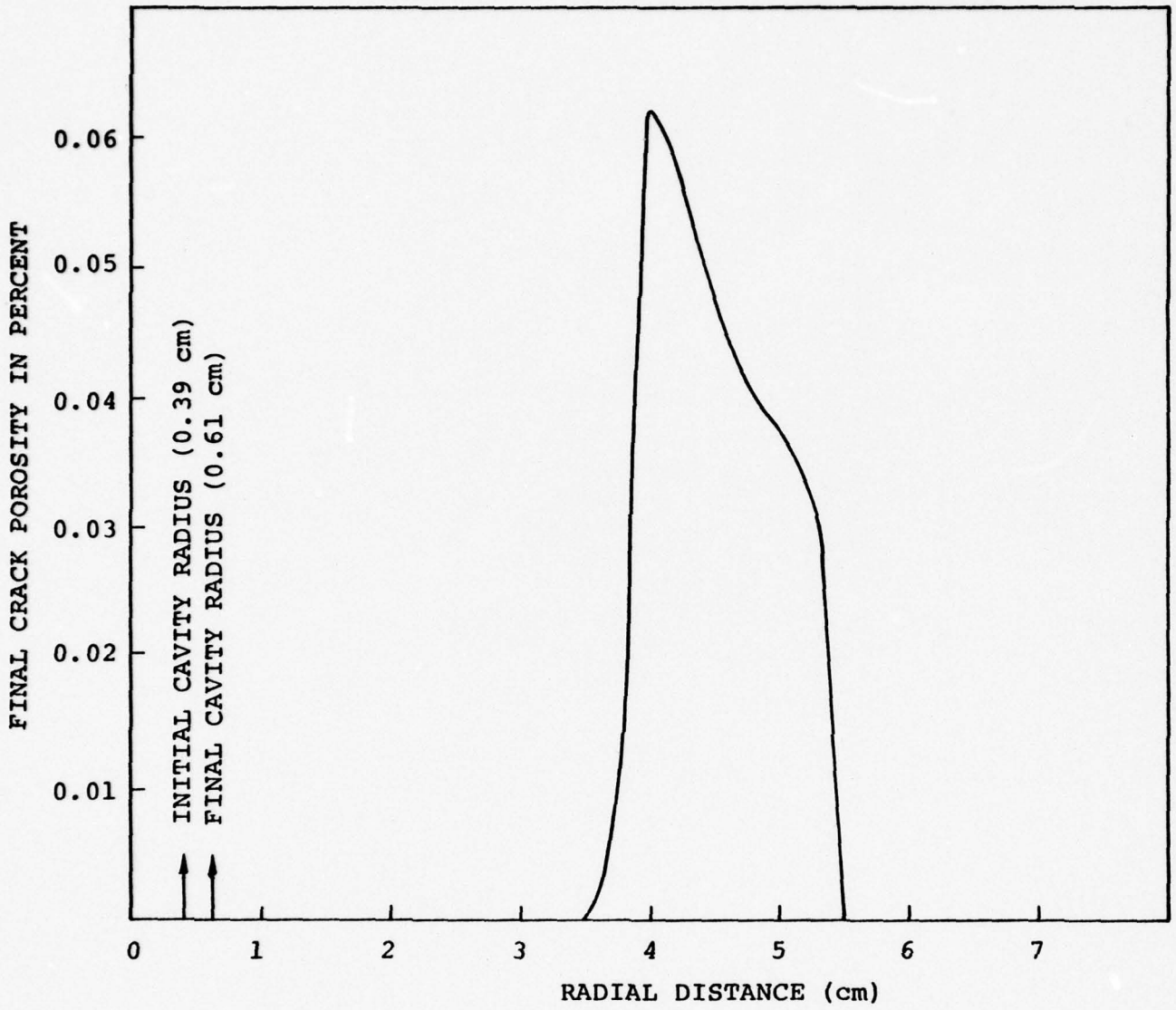

Figure 3.4. Radial distribution of crack porosity.

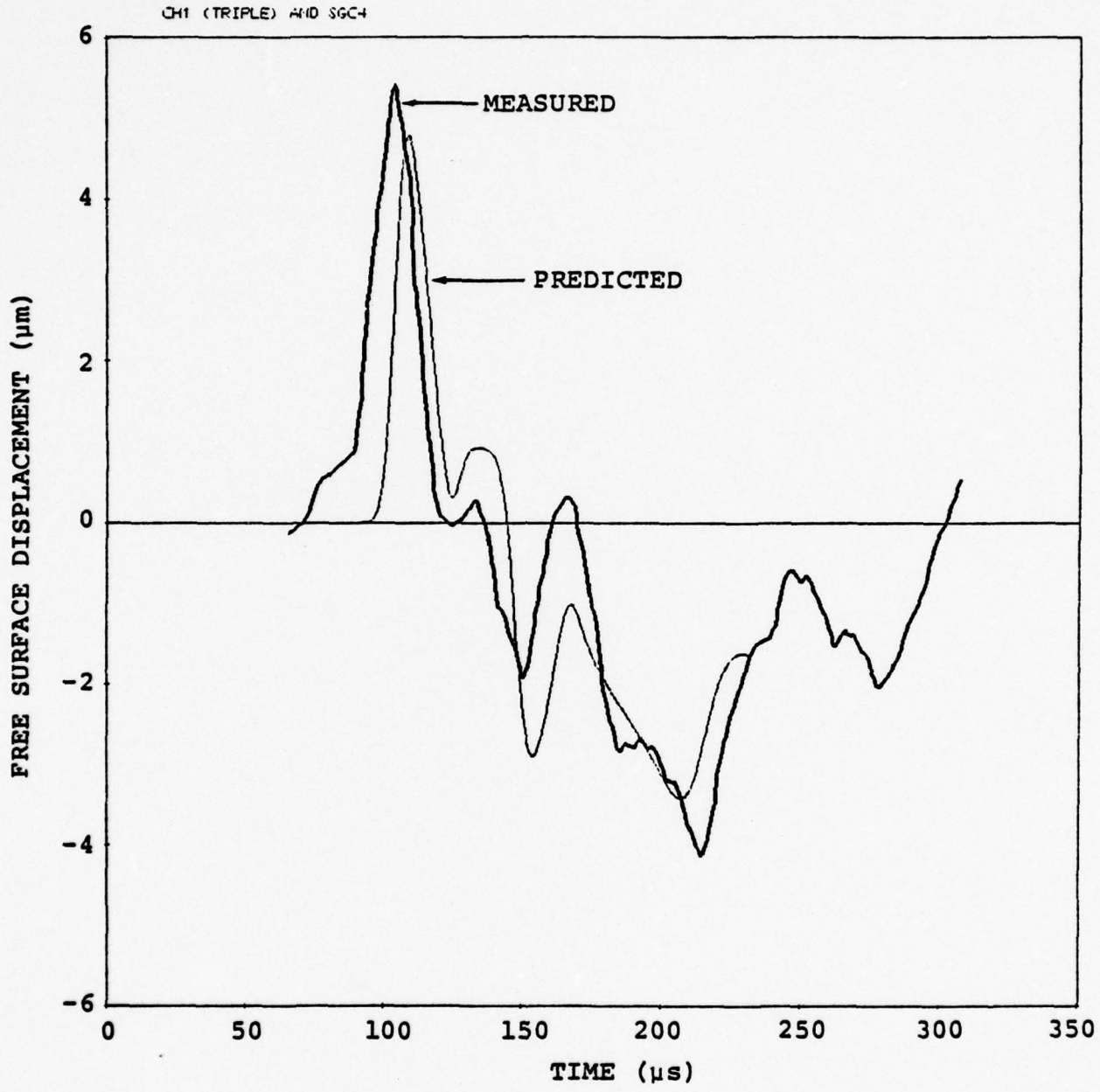

Figure 3.5. Comparison of measured and predicted displacements for Test 1. The depth of burial was 6.5 cm. The gauge was located 30.5 cm below the charge.

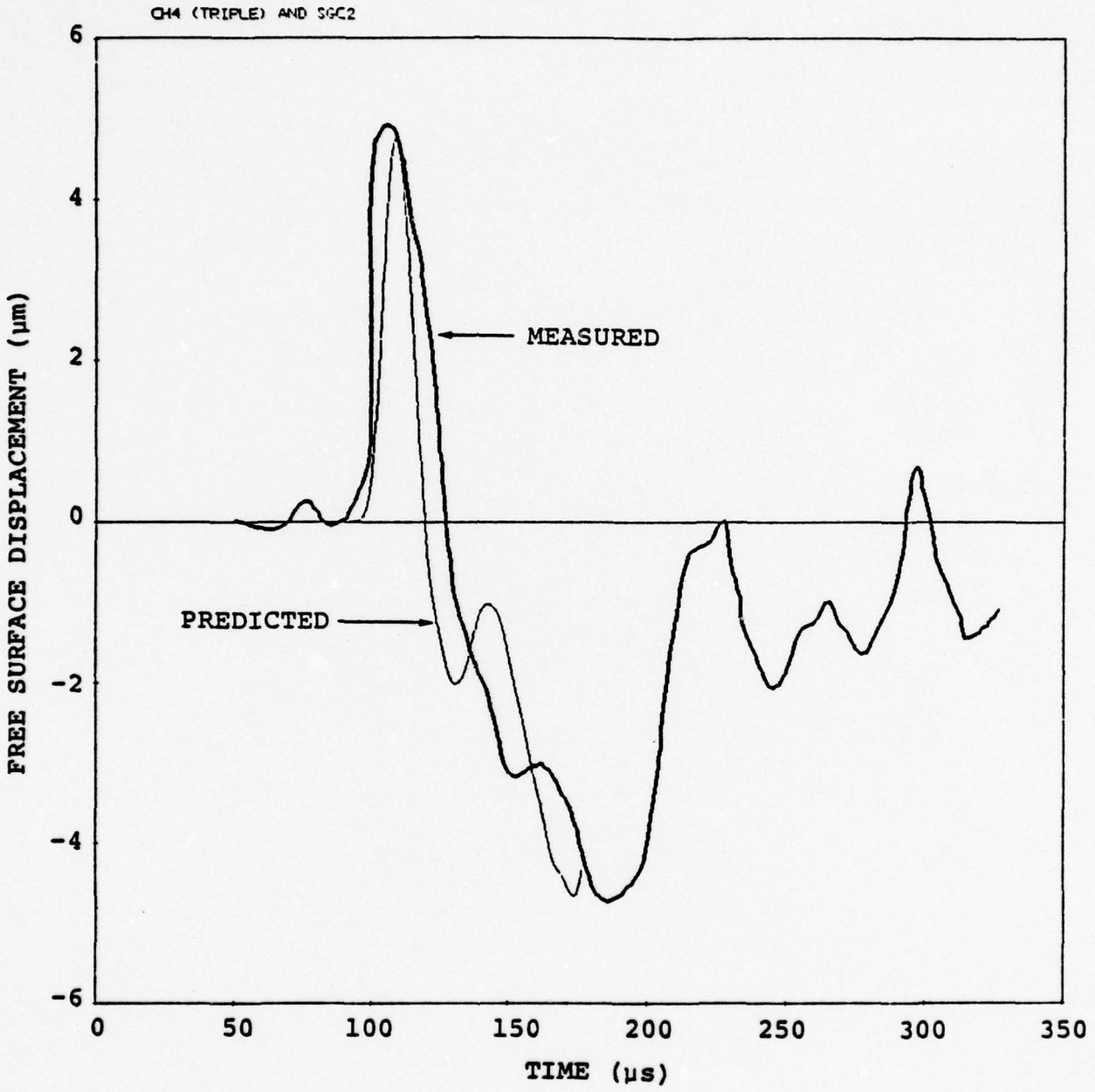

Figure 3.6. Comparison of measured and predicted displacements from the cratering shot (Test 8). The depth of burial was 1.75 cm and the crater radius was approximately 8.5 cm. The gauge was located 30.5 cm below the charge.

TABLE 3.1

MATERIAL PARAMETERS USED FOR HIGH EARLY CONCRETE

$\rho = 2.52\ g/cm^3$

$Y_u = 0.345$ kbar

$V_p = 3.00 \times 10^5$ cm/sec

$A = 93.5$ kbar

$B = 67.3$ kbar

$Y_o = 0.1725$ kbar

$Y_m = 3$ kbar

$\bar{P}_m = 5$ kbar

$G = 101.0$ kbar

$$P = A' \left(1 - \frac{\omega}{R_1 V}\right) e^{-R_1 V} + B' \left(1 - \frac{\omega}{R_2 V}\right) e^{-R_2 V} + \frac{\omega E}{V} , \quad (3.2)$$

$$P_s = A' e^{-R_1 V} + B' e^{-R_2 V} + \frac{C'}{V^{\omega+1}} , \quad (3.3)$$

where P_s is the pressure during the isentropic expansion. For Equations (3.1) and (3.2), V is the specific volume, $1/\rho$, and the constants A', B', C', R_1, R_2, and ω are given in Table 3.2.

For the numerical simulation, the source was modeled by a pressure loading function defined by Equation (3.2) and applied at the cavity boundary. The pressure function was started with the PETN detonation products expanded to the actual volume of the loose-packed PETN which corresponds to an initial radius, R_o, of 0.39 cm. Thus, the initial pressure was 31.2 kbar, which is well below the Chapman-Jouguet pressure of 320 kbars for normal density PETN.

3.4 SUMMARY

1. A complete set of calculations have been performed with depth of burial being the only variable. The results of the calculations are in good agreement with corresponding laboratory data.

2. Enough data has been saved from these calculations to analytically continue these numerical results to the far-field. A rigorous continuation procedure for a source in a halfspace is currently under development at S^3.

3. Modification of our tension fracture model was required in order to permit pP to travel through the nonlinear region surrounding the cavity.

TABLE 3.2

JWL CONSTANTS FOR PETN

$A' = 7960$ kbar

$B' = 192$ kbar

$C' = 6.65$ kbar

$R_1 = 8.50$ g/cm^3

$R_2 = 2.12$ g/cm^3

$\omega = 0.25$

$P_{cj} = 320$ kbar

$\rho_{cj} = 2.40$ g/cm^3

$\rho_{normal} = 1.77$ g/cm^3

$\rho_o = 1.0$ g/cm^3 (loosely packed)

IV. AN EXPLANATION FOR THE LARGE NEGATIVE PULSE

In Sections II and III laboratory data and numerical simulations of explosions in a halfspace were presented. All underburied shots had two events in common:

1. the direct P wave,
2. a large, low frequency arrival opposite (negative) in phase to the direct P wave.

The pP phase was depth of burial dependent. A summary of the experimental data is shown in Figure 4.1. The purpose of this section is to present an explanation for the negative pulse and examine its effect on teleseismic coupling.

The long period negative motion can be explained as an elastic effect due to near-field reflections from the free surface. The negative motion thus does not propagate to teleseismic distances. To demonstrate this, we did the following experiment. Using the reduced velocity potential from the free-field source (Figure 3.2) as a source time function, we propagated the seismic waves as though the medium were linearly elastic. The source-receiver geometry is shown in Figure 4.2.

The elastic propagation was done both numerically and analytically to eliminate the possibility of program errors. The numerical calculations were done with a finite element code. The analytic program is a generalized ray program which is capable of propagating the entire (near-field and far-field) seismic wave field (Barker, 1976).

Figure 4.3 shows the comparison between the vertical ground motion from the two-dimensional calculation described in Section III with that obtained by propagating the free-field reduced velocity potential elastically. The elastic

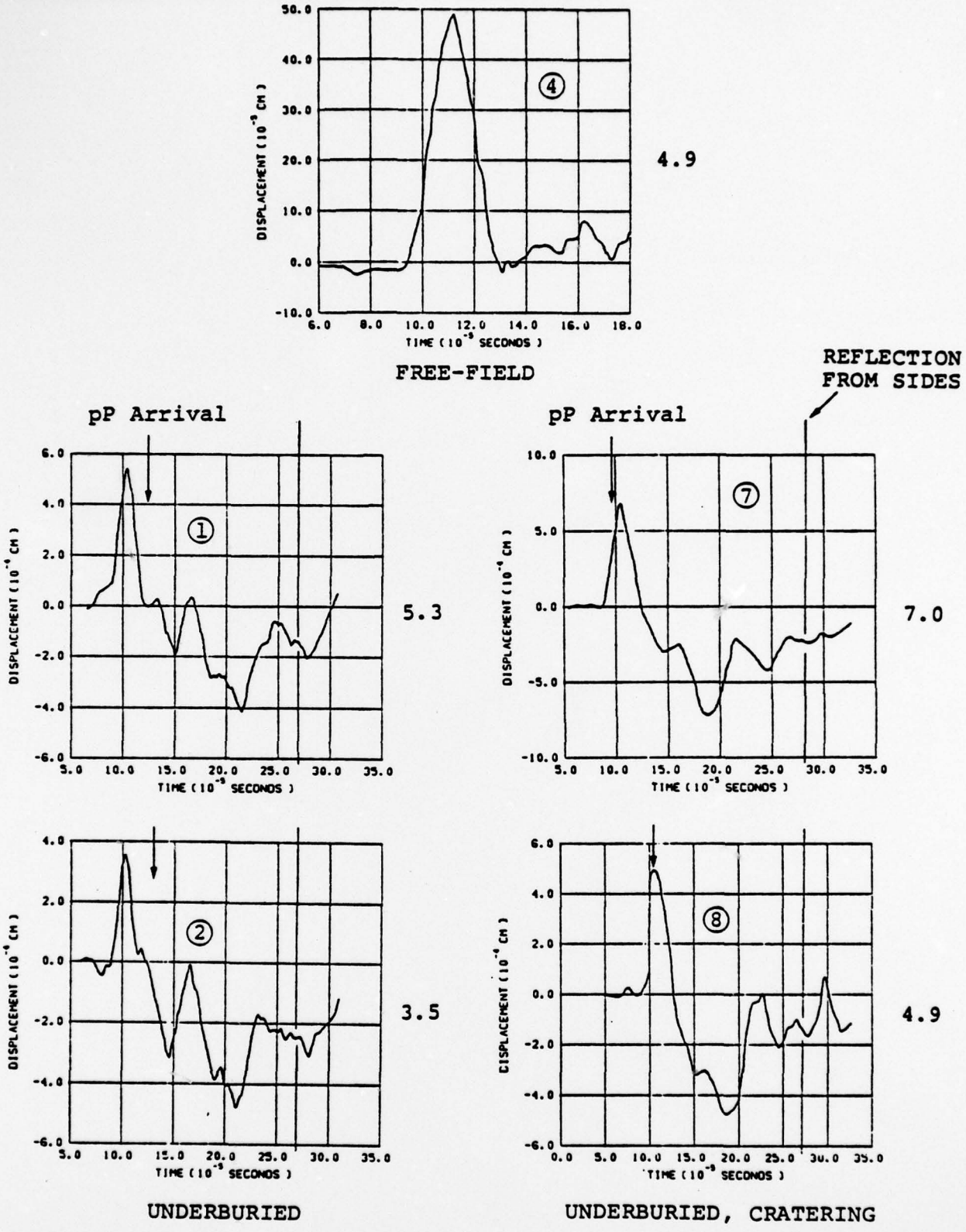

Figure 4.1. The displacement-time histories are plotted for the five experiments to be further analyzed. The test identifier from Table 3.1 is noted on each plot. At the right are the amplitudes of the peak displacement in microns. On the plots for the underburied experiments we show the expected arrival times (from elastic theory) of the free surface pP phase and the unwanted reflections from the sides of the cylinder.

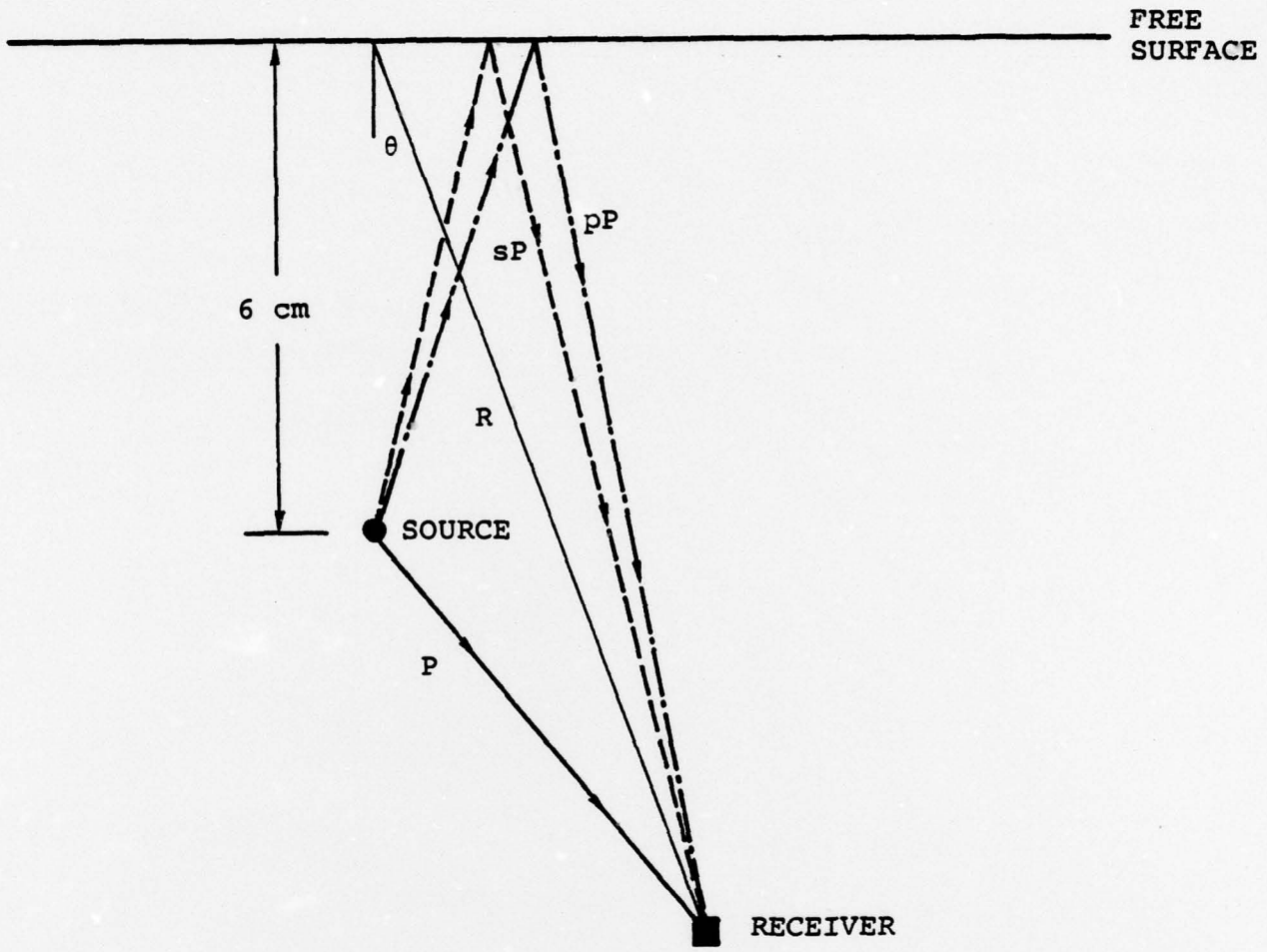

Figure 4.2. A sketch of the source-receiver geometry and ray paths is shown.

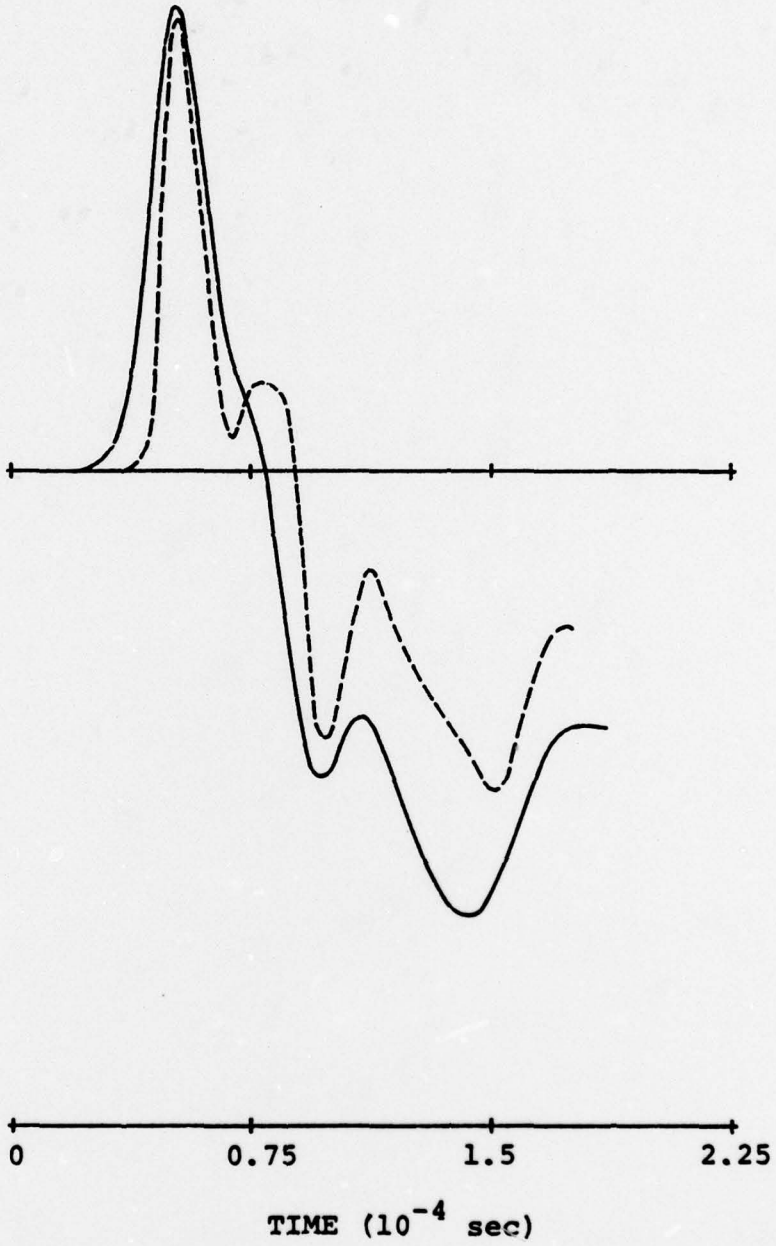

Figure 4.3. The vertical displacement from the complete two-dimensional calculation (dashed line) is compared with the displacement obtained by elastically propagating the free-field reduced velocity potential (solid line). The elastic propagation was performed numerically using the RVP of Figure 3.2 as a source.

propagation was done numerically using a finite element code. In this case $\theta = 0$ and the receiver is located on a bottom free surface at a depth of 30 cm. We see that the signals are very much alike. In particular, they both exhibit the long period negative pulse mentioned above. We may therefore conclude that this pulse is due to elastic propagation effects.

In order to understand the elastic propagation effects, we turn to the generalized ray calculations. These calculations allow one to examine separately the contributions of the direct P and reflected pP and pS phases. Figure 4.4 shows sketches of the Green's functions (δ-function responses) for vertical displacement for a typical source-receiver geometry. The figure shows the signals separately and combined. The direct P wave begins as a pulse followed by a plateau, which is the near-field P contribution. The pP phase begins as a pulse, but we note that the near-field part of this signal is a negative ramp, which is typical of near-field reflections. This is an effect due to a spherical wave reflecting from a flat impedance contrast, in this case the free surface. The near-field ramp of the pS phase adds to the pP ramp to produce a static offset. For $\theta = 0$, there is no far-field pS wave, but there is a near-field term.

The Green's functions were convolved with the free-field reduced velocity potential. An example is in Figure 4.5 shown for $\theta = 4°$, R = 30 cm. The shape of the signal is very much like those in Figure 2.2. Here we can identify the long period negative pulse with the negative ramp between the pP and sP arrival times.

To show how the waveform develops and how it propagates to teleseismic distances, we have computed the signal along a teleseismic ray path, $\theta = 20°$, for increasing values of R (Figure 4.6). For small values of R, the negative pulse is not apparent because the sP - pP time is too short. As this

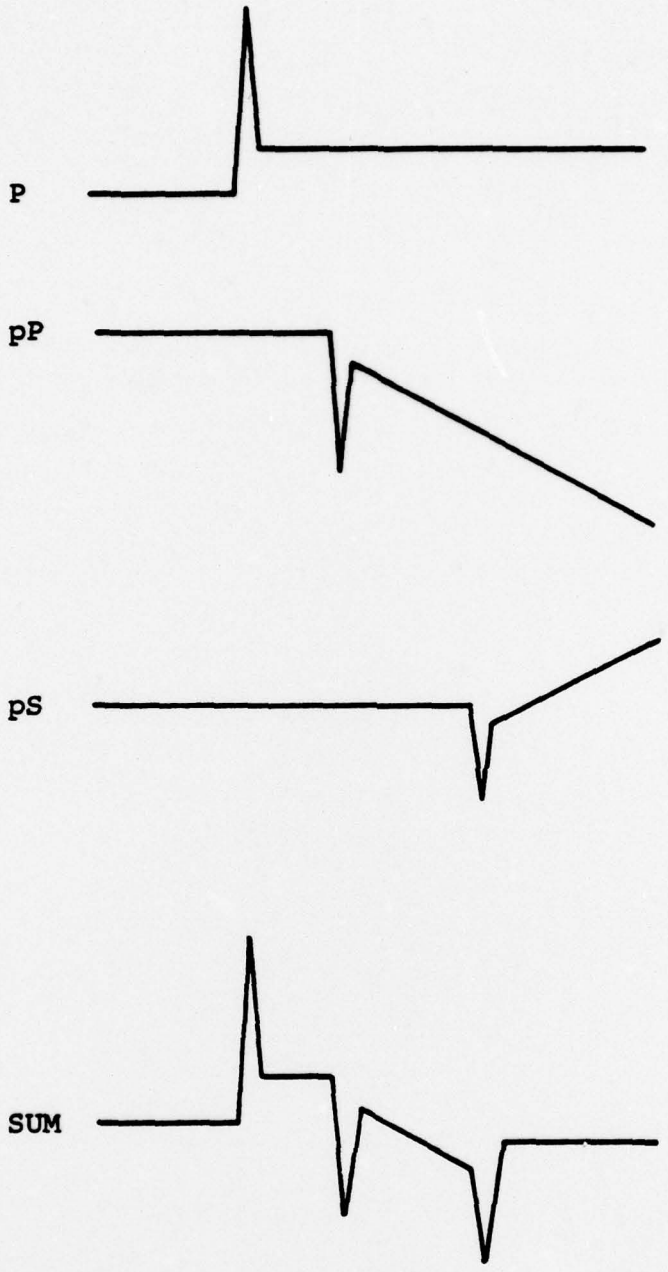

Figure 4.4. A sketch of the Green's function is shown.

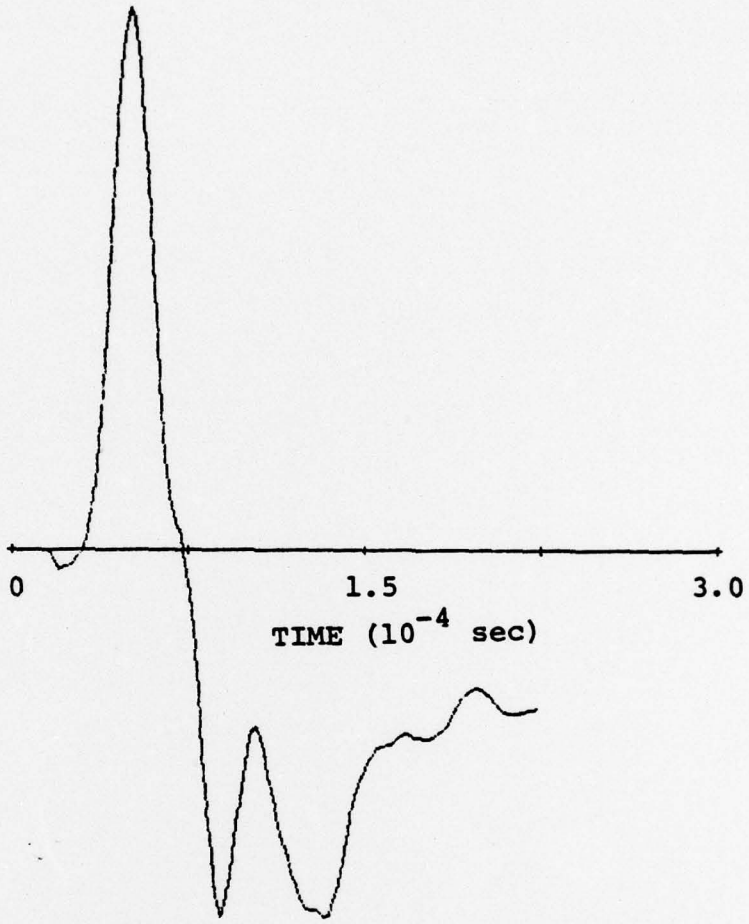

Figure 4.5. The vertical displacement is shown for $\theta = 4°$, R = 30 cm. The reduced velocity potential is propagated using the analytic generalized ray program.

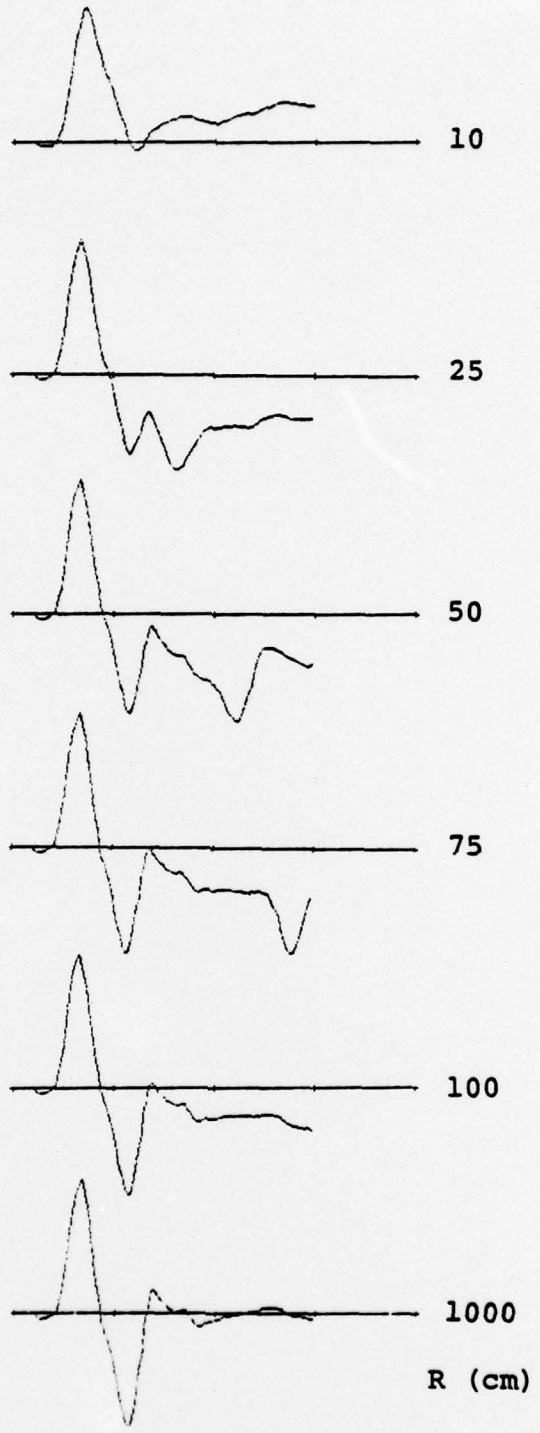

Figure 4.6. Vertical displacements are shown along the ray $\theta = 20°$. Tick marks are 0.75×10^{-4} sec apart.

time difference increases, the long period negative pulse becomes prominent. At larger ranges, the pP near-field term becomes small. At teleseismic ranges, the negative pulse is absent and has no effect on measurements of m_b or M_s. These results make clear the importance of using the appropriate Green's function when extrapoling near-source numerical solutions to the far-field.

V. SUMMARY AND RECOMMENDATIONS

1. The free-field RVP spectrum for an explosion in concrete was observed to be mildly peaked, with the difference between the spectral peak and Ψ_∞ corresponding to 0.09 magnitude units.

2. We were able to obtain an excellent match to the free-field data by using published data for the material properties of concrete, our own measurements of P velocity and unconfined compressive strength and published data for PETN.

3. The large, long period negative pulse was observed on all underburied shots in both the laboratory data and the numerical simulation, whether or not spall and/or cratering occurred at the free surface. Our explanation of this pulse is that it is a near-field wave produced by a spherical P wave reflecting from a plane impedance contrast. It should not propagate to the far-field.

4. We were able to obtain an acceptable match to the underburied shot data only after modifying the tension failure model. This modification somewhat degraded the match to the free-field data.

5. The calculational results indicate that tension failure is required to produce a peaked spectrum. However the distinct pP arrival observed in the data suggest that these fractures either do not remain open or else fill with water. It would be interesting to section the concrete blocks and observe the degree of fractures produced in each experiment.

6. Sufficient data from each calculation has been saved in order to analytically continue the close in ground motion to the far-field. Rigorous analytic continuation

algorithms for sources in a halfspace are being developed at S^3. They will be used to determine the effect of depth of burial on teleseismic ground motion using the data obtained under this contract.

7. The laboratory modeling work should be extended to include multiple charge, decoupling and asymmetrical cavity studies.

8. We should perform free-field experiments in real rocks, e.g., granite, sandstone, shale and salt, both saturated and dry where possible, using the experimental techniques developed under this contract.

REFERENCES

Barker, T. G., [1976], "Calculation of the Effects of Layered Geology on Near-Field Ground Motions Using a Hybrid Finite Difference/Linear Elastic Code for the NTS MIGHTY EPIC Event," Systems, Science and Software Topical Report SSS-R-76-2914 submitted to the Defense Nuclear Agency, May 1976.

Cherry, J. T. and F. L. Petersen, [1970], "Numerical Simulation of Stress Wave Propagation From Underground Nuclear Explosions," Engineering With Nuclear Explosives, Vol. I., 142-173, January 1970.

Cherry, J. T., N. Rimer and W. O. Wray, [1975], "Seismic Coupling From a Nuclear Explosion: The Dependence of the Reduced Displacement Potential on the Nonlinear Behavior of the Near Source Rock," Systems, Science and Software Technical Report SSS-R-76-2742, ARPA Contract No. F08606-75-C-0045, September 1975.

Erlich, D. C., [1975], "Three-Dimensional Seismic Modeling," Stanford Research Institute Report, SRI Project PYU-3287.

Finger, M., F. Helm, E. Lee, R. Boat, H. Chering, J. Walton, B. Hayes, and L. Penn, [1976], "Characterization of Commercial Composite Explosives," preprint from The Sixth Symposium on Detonation